
1 The FY-3D Global Active Fire product: Principle, 2 Methodology and Validation

3 Jie Chen^{1,2-†}, Qi Yao^{3,2-†}, Ziyue Chen^{3,2*}, Manchun Li^{4,2}, Zhaozhan Hao^{5,4}, Cheng Liu^{1,2}, Wei
4 Zheng^{1,2}, Miaoqing Xu^{3,2}, Xiao Chen^{3,2}, Jing Yang^{3,2}, Qiancheng Lv^{3,2}, Bingbo Gao^{5,4*}

5 ¹ Innovation Center for FengYun Meteorological Satellite, National Satellite Meteorological Center
6 (National Center for Space Weather), China Meteorological Administration, Beijing 100081, China

7 ² Key Laboratory of Radiometric Calibration and Validation for Environmental Satellites, National
8 Satellite Meteorological Center (National Center for Space Weather), China Meteorological
9 Administration, Beijing 100081, China

10
11 ^{3,2} College of Global Change and Earth System Science, Beijing Normal University, Beijing 100091,
12 China

13 ^{4,2} School of Geography and Ocean Sciences, Nanjing University, Nanjing 210008, China

14 ^{5,4} College of Land Science and Technology, China Agricultural University, Beijing 100083, China

15 †These authors contributed equally.

16 *Correspondence to: Ziyue Chen (zychen@bnu.edu.cn) or Bingbo Gao (gaobingbo@cau.edu.cn)

17 **Abstract.** Wild fires have a strong negative effect on environment, ecology and public health. However,
18 the potential degradation of mainstream global fire products leads to large uncertainty on the effective
19 monitoring of wild fires and its influence. To fill this gap, we produced FY-3D global fire products with
20 a similar spatial and temporal resolution, aiming to serve as the alternative and continuity and
21 replacement for MODIS global fire products. Firstly, the sensor parameters and major algorithms for
22 noise detection and fire identification in FY-3D products were introduced. For visual-check-based
23 accuracy assessment, five typical regions, Africa, South America, Indo-China Peninsula, Siberia and
24 Australia, across the globe were selected and the overall accuracy exceeded 94%. For accuracy
25 assessment, five typical regions, Africa, South America, Indo-China Peninsula, Siberia and Australia,
26 across the globe were selected. The overall consistence between FY-3D fire products and reference data
27 exceeded 94%, with a more than 90% consistence in all regions. Furthermore Meanwhile, the consistence
28 between FY-3D and MODIS fire products was examined. The result suggested that the overall
29 consistence was 84.4%, with a fluctuation across seasons, surface types and regions. The high accuracy
30 and consistence with MODIS products proved that FY-3D fire product was an ideal tool for global fire
31 monitoring. Based on field-collected reference data, we further evaluated the suitability of FY-3D fire
32 products in China. The overall accuracy and accuracy (without considering omission errors) was 79.43%
33 and 88.50% respectively, higher than that of MODIS fire products. Specially, since detailed local
34 geographical conditions in China were specifically considered, FY-3D products should be preferably
35 employed for fires monitoring in China. FY-3D fire dataset can be downloaded at
36 <http://satellite.nsmc.org.cn/portalsite/default.aspx> (NSMC, 2021).

37 1 Introduction

38 More than half of global land surfaces have been influenced by wild fires and the total global burned area
39 summed up to the area of European Union every year (Andela et al., 2019; Keeley et al., 2011; Moritz et
40 al., 2012). Wild fires, especially large-scale wild fires, in forests, grasslands and farmlands have a
41 significant impact on crop productivity (Jethva et al., 2019), atmospheric pollution (Guo et al., 2020),
42 biodiversity (Kelly et al., 2020), climate change (Alisjahbana et al., 2017; Keegan et al., 2014) and public
43 health (Huff et al., 2015; Johnston et al., 2012; Oliveira et al., 2020; Yuchi et al., 2016). In recent years,
44 the increasing events of forest fires in China, US, Australia, and Amazon Rain Forests and grassland fires
45 in Mongolia have caused a large number of casualty (Cochrane, 2003), ~~the lost millions of millions of~~ forest
46 wildlife (Wintle et al., 2020), remarkably deteriorated air quality (Guo et al., 2010; Liu et al., 2018;
47 Marlier et al., 2012; Volkova et al., 2019), severely damaged ecosystems (Cerdeira et al., 2012), massive
48 economic losses (Stephenson et al., 2013) and regional or global climate change (Abram et al., 2021;
49 Jacobson, 2014; Twohy et al., 2021; Wang et al., 2020).

50
51 Due to its great influences, growing emphasis has been placed on the monitoring of wild fires based on
52 remote sensing products. Since 1970s, the implementation and research of satellite-based fire detection
53 has started in US using National Oceanic and Atmospheric Administration (NOAA) series satellites
54 (www.noaa.gov, Dozier et al., 1981; Flannigan and Haar et al., 1986; Kaufman et al., 1990; Boles et al.,
55 2000). NOAA fire products, with a spatial resolution of 1.1 km and a daily temporal resolution, have
56 been employed globally for decades, and provide the data support for long time series analysis. In
57 addition to NOAA fire products, a diversity of regional or global fire products has been proposed in
58 recent years.

59
60 Thanks to its easy access, long time series, and reliable accuracy (Giglio et al., 2018), the Moderate
61 Resolution Imaging Spectroradiometer (MODIS) fire product, with a spatial resolution of 1km and a
62 temporal resolution of 12 hours, have been available since 2000 and become one of the most widely
63 employed fire products to monitor the temporal evolution of large-scale wide fires, including forest fires
64 (Mohajane et al., 2021), grassland fires (Zhang et al., 2017) and crop residue burning (Li et al., 2016).
65 With a similar temporal resolution (12 hours), the Visible Infrared Imaging Radiometer Suite (VIIRS)
66 fire products with a spatial resolution of 375m has been available for fire detection since 2011. Despite
67 a higher spatial resolution, VIIRS fire products are produced using less bands than MODIS fire products,
68 and the mainly used 4- μm I-band may lead to large bias in the estimation of FRP (Fire Radiative Power)
69 during an intense fire event (Schroeder et al., 2014). Consequently, VIIRS fire products present a
70 relatively poor consistence with MODIS fire products and the accuracy of VIIRS fire products is
71 generally lower than that of MODIS fire products (Sharma et al., 2017). In this case, VIIRS fire products
72 may not serve as a complete replacement of and should be comprehensively employed with MODIS fire
73 products. ~~Available since 2013, Landsat fire products employ the visible and near-infrared (VNIR) and
74 short-wave infrared (SWIR) bands of the Landsat 8 imagery to detect thermal anomalies (Kumar and
75 Roy, 2017; Murphy et al., 2016; Schroeder et al., 2016). Its spatial and temporal resolution is 30 m and
76 16 days, respectively. Despite its fine spatial resolution, its coarse temporal resolution makes this data~~

~~source not suitable for monitoring the occurrence and evolution of wild fires. Instead, Landsat fire products are more frequently employed for identifying the post-fire areas.~~

In recent years, with the growing needs for real-time monitoring of a diversity of environmental issues and ecological process, some satellites have been launched to provide remote sensing products with extremely high temporal resolution. GEOS-16 Advanced Baseline Imager (ABI) active fire products, with a temporal resolution of five minutes and a spatial resolution of 2km, have been available since 2017 (Hall et al., 2019). GEOS-ABI fire products can effectively monitor middle to large-scale fires and be used for estimating fire emissions. GEOS-ABI fire products may lead to a poor detection accuracy when identifying small-scale fires (Li et al., 2020). GEOS-ABI mainly provides regional fire products in Southeastern Conterminous United States (CONUS). Himawari-8 products, with a spatial resolution of 2 km and temporal resolution of 10 minutes, have been widely employed to monitor meteorology and wild fires in Asia and Australia since 2015 (Xu et al. 2017). Similar to GEOS-16 ABI fire products, Himawari-8 fire products are also limited in effectively detecting small-scale fires (Wickramasinghe et al., 2018). Despite an extremely high temporal resolution, fire products produced using geostationary satellites only cover a regional area and cannot monitor the distribution and evolution of wild fires at a global scale.

~~Long-term running leads to the aging of sensors (Sayer et al., 2015; Liu et al., 2017; Barnes et al., 2019) and causes the degradation of sensor sensitivities (Lyapustin et al., 2014; Doelling et al., 2015; Xiong et al., 2019), increased system errors (Fensholt et al., 2012; Xie et al., 2011) and decreased product quality (Fang et al., 2012; Wang et al., 2012). Suits et al., 1988; Lyapustin et al., 2014; Fensholt et al., 2012; Wang et al., 2012. With a high temporal resolution and so far the longest time series, MODIS global fire products have become the most important data source for examining historical regional and global fires, monitoring occurring fires, and investigating their environmental influences. However, after twenty-two years' running, the gradual ageing of sensors will, if not already, cause the future degradation of MODIS global fire products. To continuously make full use of the existing long-term series of MODIS fire product, even if it degrades or stops services in the future, a fire product with good reliability, good consistence and similar characteristics is urgently needed to serve as the potential alternative and continuity of global MODIS fire products. With the ageing of existing mainstream global fire monitors (e.g. MODIS), their accuracy and reliability presented a notable decrease (Wang et al., 2012) and can no longer provide high quality data for effective fire monitoring and a series of relevant studies. Therefore, there is a growing need for alternative global fire products. Since the launch of Fengyun-3C (FY-3C) satellite in September, 2013, a series of FY meteorological satellites have been designed to produce global active fire products. FY-3C VIRR fire products were produced based on an effective active fire detection algorithm (Lin et al., 2017), which considered dynamic thresholds and infrared gradients. However, the overall accuracy of FY-3C VIRR fire products remained unsatisfactory at the global scale and are thus not publicly released.~~

带格式的：段落间距段前：0.5 行

116
117 In November, 2017, Fengyun-3D (FY-3D) satellite was launched with an improved Medium Resolution
118 Spectral Imager (MERSI) for fire detection. ~~With a similar spatiotemporal resolution, FY-3D, which~~
119 provides a promising solution for ~~replacing existing fire products~~ the continuity of global MODIS fire
120 products. In this paper, we introduce the characteristics and fire detection algorithms of a new global fire
121 products based on FY-3D (recently downloadable from our official website
122 <http://satellite.nsmc.org.cn/portalsite/default.aspx>). ~~Through visual check, consistence check and~~
123 accuracy assessment based on ground-truth data, FY-3D global fire product ~~Furthermore, this fire product~~
124 is comprehensively compared with ~~the other mainstream fire products, especially~~ MODIS global fire
125 products at the global and regional scale. Thanks to its good global consistence and regional suitability.
126 ~~The new~~ FY-3D global fire products has the potential to aim to serve as a continuity of ~~the global existing,~~
127 ~~yet degrading~~ MODIS fire products and better support ~~regional (especially Asia) and global~~ ecological
128 and environment research in China.

129 2 The overview of FY-3 fire products

带格式的：段落间距段前：12 磅，段后：6 磅

130 2.1 Instrument

131 As one of the core instruments of the Fengyun-3 (FY-3) satellite, the updated medium resolution spectral
132 imager (MERSI) ~~can be comparable with the imaging instrument of the latest polar orbiting~~
133 ~~meteorological satellite launched by the United States, and~~ has become one of the most advanced remote
134 sensing instruments based on wide swath imaging. FY-3D satellite was launched in November 2017 with
135 10 sets of remote sensing instruments, including the medium resolution spectral imager (MERSI-II),
136 ~~microwave temperature sounder (MWTS II), microwave humidity sounder (MWHIS II), hyper spectral~~
137 ~~infrared atmospheric sounder (HIRAS), microwave radiation imager (MWRI), near-infrared hyper~~
138 ~~spectral greenhouse gas monitor (GAS), wide angle aurora imager (WAI I), iono spheric photometer~~
139 ~~(IPM), space environment monitor (SEM), and global navigation occultation sounder (GNOS) (National~~
140 ~~Satellite Meteorological Center, 2010).~~

141
142 MERSI-II integrates the functions of the original two imaging instruments (MERSI-I and VIRR) of FY-
143 3B and FY-3C, with a total of 25 channels, including visible light, near infrared, medium infrared, and
144 far infrared (As Table 1). The infrared imaging, detection sensitivity, and calibration accuracy of MERSI-
145 II are improved greatly. It is the first imaging instrument that can access the 250-meter resolution
146 infrared split-window area globally and capture seamless 250-meter resolution true color global images
147 on a daily basis. MERSI-II also enables the high-quality retrieval of atmospheric, land, and marine
148 parameters such as clouds, aerosols, vapor, land surface features, and ocean color, supporting global
149 support for environment and climate issues.

带格式的：两端对齐，行距：1.5 倍行距，无孤行控制

151 **Table 1** Major channel parameters of FY-3D/MERSI-II (Compared with MODIS/Aqua) channel
152 parameters

Channel	Wavelength/ μm	Waveband	Resolution/km	Application
---------	---------------------------	----------	---------------	-------------

MERSI	MODIS	MERSI	MODIS	MERSI	MODIS	MERSI	MODIS	
1	3	0.470	0.469	Visible light		0.25	0.50	Ocean Color/
2	4	0.550	0.555	Visible light		0.25	0.50	Land
3	1	0.650	0.645	Visible light		0.25	0.25	Land/Cloud
								Ocean
4	2	0.865	0.859	Near infrared		0.25	0.25	Color/Vegetation
5	5	1.380	1.380	Near infrared		1.00	0.50	Land/Cloud/
6	6	1.640	1.640	Near infrared		1.00	0.50	Snow
7	7	2.130	2.130	Near infrared		1.00	0.50	Land/Cloud
8	8	0.412	0.412	Visible light		1.00	1.00	
9	9	0.443	0.443	Visible light		1.00	1.00	
10	10	0.490	0.488	Visible light		1.00	1.00	
11	12	0.555	0.555	Visible light		1.00	1.00	Ocean Color/
12	13	0.670	0.667	Visible light		1.00	1.00	Phytoplankton/
13	—	0.709	—	Visible light		1.00	—	Biogeochemistry
14	15	0.746	0.748	Visible light		1.00	1.00	
15	16	0.865	0.869	Near infrared		1.00	1.00	
16	17	0.905	0.905	Near infrared		1.00	1.00	Atmosphere/
17	18	0.936	0.936	Near infrared		1.00	1.00	Water Vapor
18	19	0.940	0.940	Near infrared		1.00	1.00	
19	26	1.040	1.040	Near infrared		1.00	1.00	Cirrus
20	20	3.800	3.750	Medium infrared		1.00	1.00	Surface/Cloud/
21	23	4.050	4.050	Medium infrared		1.00	1.00	Atmospheric
								Temperature
22	28	7.200	7.325	Far infrared		1.00	1.00	Water Vapor
23	29	8.550	8.550	Far infrared		1.00	1.00	
24	31	10.800	11.030	Far infrared		0.25	1.00	Surface/Cloud
25	32	12.000	12.020	Far infrared		0.25	1.00	Temperature

带格式表格

153 **2.2 Product overview**

154 There are two middle-infrared band (3.8um and 4.05um) and both middle-infrared band (3.8um and
155 4.05um) are sensitive to strong heat signals. Their differences lie in their performance under different
156 temperature and radiation conditions. 3.8um is more close to the wavelength of solar radiation, and has
157 better reflection under solar radiation. As a comparison, 4.05um is more easily to miss weak fires.
158 Therefore, current FY-3D fire products are mainly produced based on 3.8um band for better fire
159 identification. The global fire monitoring by FY-3D satellite is mainly based on the sensitivity of MERSI-
160 II Channel 20 (mid infrared channel) to high temperature heat sources (fire spots). According to the
161 calculation, the emissivity of forest and grassland fires in the mid-infrared band can be hundreds of times
162 higher than that of the surface at normal temperature, making the radiance and brightness temperature of

163 the fire-spot significantly higher than surrounding pixels. For rapid monitoring of global wildfires, it is
164 necessary to develop an algorithm for the automatic identification of fire spots.

165
166 MERSI-II fire monitoring products from FY-3D satellite can provide fire spot location, sub-pixel fire
167 spot area, temperature, and fire spot intensity, in inland areas around the world and generate global fire-
168 spot pixel information (including day and night) in an HDF format. FY-3D fire products are produced
169 following a projection with the equal latitude and longitude (0.01 °). Fire spot intensity is classified
170 according to sub-pixel fire spot area and temperature, with an overall accuracy above 85%. Based on
171 daily monitoring products, SMART (Satellite Monitoring Analyzing and Remote sensing Tools) system
172 can generate the images of global monthly fire spot distribution, with a resolution of 0.25 °.

173
174 The algorithm for fire spot identification depends on the sensitivity of mid-infrared channels to high-
175 temperature heat sources. The radiance and brightness temperature of the pixels in the mid-infrared
176 channels with sub-pixel fire spots are higher than those of the surrounding non-fire pixels and those of
177 the pixels in the far-infrared channels. Therefore, the pixels with fire spots can be identified by setting
178 an appropriate threshold, and the estimation of background temperature is the key to high detection
179 accuracy and sensitivity.

180
181 Sub-pixel fire spot estimation relies on the brightness temperature in mid-infrared channels, and the far-
182 infrared channels are employed when the mid-infrared channels have saturated brightness temperature.
183 In the single-channel estimation formula, the temperature of the open flame spot is set to 750 K.

184
185 Fire spot intensity, namely fire radiation power (FRP), is obtained by substituting the area and
186 temperature of sub-pixel fire spots into the Stephen-Boltzmann formula of full-band blackbody radiation.

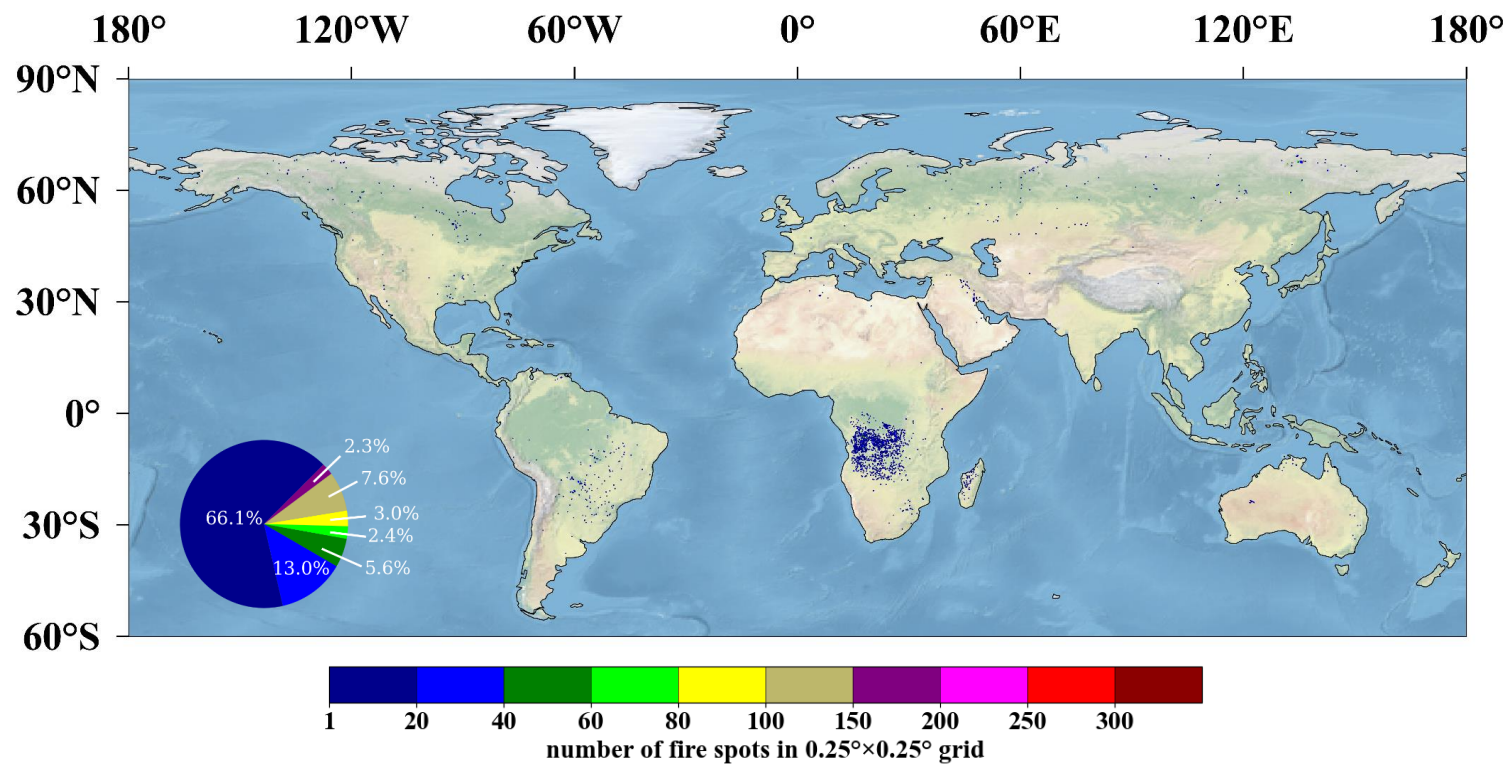
187 $J^* = \varepsilon\sigma T^4$, (1)
188

189 The radiant emittance J^* has dimensions of energy flux, and the SI units of measure are joules per second
190 per square meter. The SI unit for absolute temperature T is the kelvin. ε is the emissivity for the grey
191 body; if it is a blackbody, $\varepsilon = 1$. σ is the Stephen-Boltzmann constant.

192
193 FRP is divided into 10 levels, indicating different ranges of radiation intensity and the fire behavior at
194 fire-spot pixels. Fire spots are classified into four groups with regard to credibility, namely the real fire
195 spots, possible fire spots, fire spots affected by the cloud and noisy (fire spots disturbed by clouds and
196 noise).

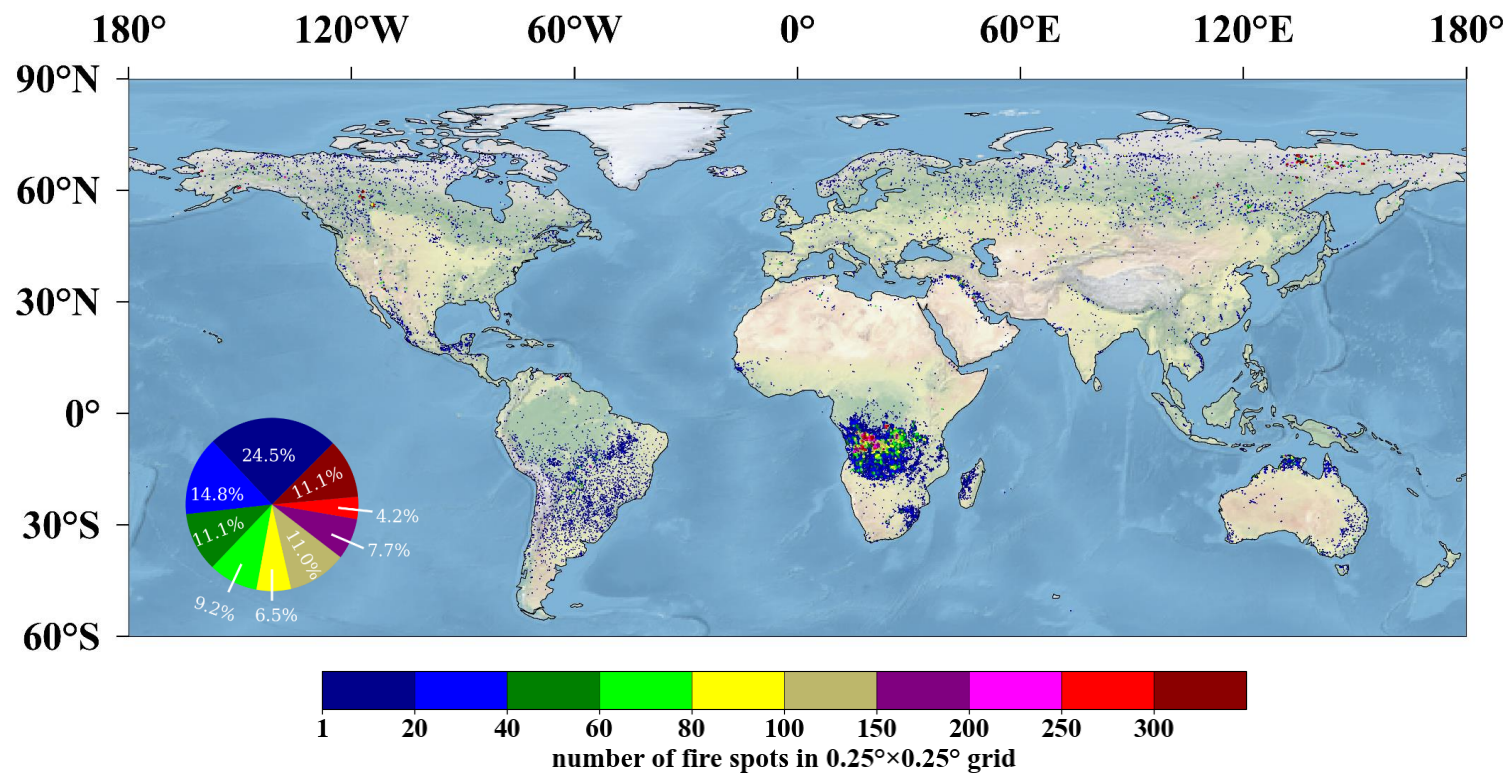
197
198 FY-3D/MERSI-II daily global fire monitoring products is illustrated in Fig. 1. The major processing of
199 daily fire spot products is the generation of 5-minute fire spot lists, which includes such information as
200 observation time of fire spot pixels, latitude and longitude, sub-pixel fire spot area and temperature, and
201 FRP. Next, all the 5-minute fire spot information for each day is merged into the daily global fire
202 information list.

203
204 FY-3D/MERSI-II monthly global fire monitoring products consist of the information list of global fire
205 spot pixels and the density map of global fire spots. The information list of monthly global fire spots
206 covers all global fire spot pixels in this month. Concerning the multi-time monitoring information of the
207 same pixel, the maximum fire spot area is taken as the current-month fire spot information for the pixel.
208 Fig. 2 is an illustration of the density map of global fire spots based on FY-3D/MERSI-II, in which
209 different colors indicate the number of fire spot pixels at $0.25^{\circ} \times 0.25^{\circ}$ spatial grid. Compared with daily
210 FY-3D fire products, monthly FY-3D fire products were advantageous of revealing the global patterns of
211 fire spots. As shown in Fig. 2, the global fire spots were mainly distributed in southern Africa, central
212 South America, southern North America, north-central Asia, and northern Australia in June, 2019.



213

214 **Figure 1** Thematic map of global fire monitoring by FY-3D (2019-06-13). The color bar with different colors means the number of fire spots in the 0.25° x 0.25° grid.



215

216 **Figure 2** Density map of global fire spots based on FY-3D (2019-06). Fire-prone areas ~~are~~were distributed in northern Russia, south-central Africa, southeastern South America,
 217 coastlands of Australia and small parts of Canada.

218 **3 Methods**

219 This section mainly introduces the specific algorithm and steps for generating FY-3D global fire products
220 based on the original data obtained from MERSI-II. The input data include MERSI-II global orbital
221 Earth observations, MERSI-II global orbital geographical locations, MERSI-II global orbital cloud
222 detection data, and global land and sea template data, as shown in Table 2.

223 **Table 2_** Input file list of MERSI-II global fire monitoring software.

No.	Item	Format	Data type	Period	Source	Description
1	MERSI-II global orbital Earth observations	hdf	1B	Real-time	Preprocessor	Data file after preprocessing 5-minute data segments of MERSI-II
2	MERSI-II global orbital geolocations	hdf	Float	Real-time	Preprocessor	Locations after preprocessing 5-minute data segments of MERSI-II
3	MERSI-II global orbital cloud detection data	hdf	Float	Real-time	Product system	5-minute cloud detection products of MERSI-II produced by the product system
4	Global land and sea template data	dat	Grid	Static	Data management and user service subsystem	Global land-sea boundaries

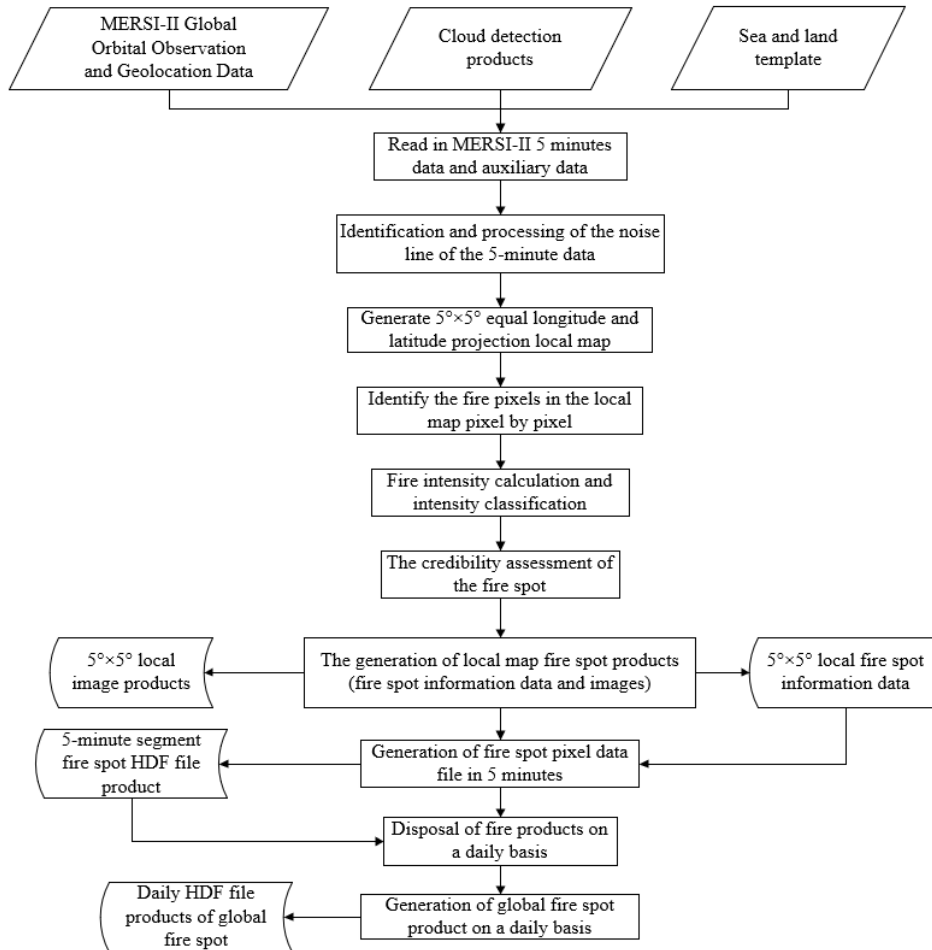
224
225 Automatic identification of fire spots is the major step for generating fire products. Firstly, the 5-minute
226 L1 data segments of MERSI-II and various auxiliary data are read in, and the noise lines are identified
227 to generate the noise line mark. Next, the 5-minute data segments are projected according to rule of the
228 equal latitude and longitude, and cut as $5^{\circ} \times 5^{\circ}$ grids to generate a local map.

229
230 Secondly, fire spots in each $5^{\circ} \times 5^{\circ}$ local map are identified pixel by pixel, subject to the calculation of
231 sub-pixel fire spot area and the estimation of FRP. According to the credibility, the identified fire spot
232 pixels are classified into four categories. Subsequently, all the $5^{\circ} \times 5^{\circ}$ local fire spot information in the
233 5-minute data segments is synthesized to generate fire-spot HDF file products. The general steps for
234 producing FY-3D fire products is briefly explained in Fig 3 and the detailed procedures are explained as
235 follow.

带格式的: 段落间距段前: 12 磅

带格式的: 居中

带格式表格



236
 237 **Figure 3** General flow chart ~~of the processing algorithm~~ for generating FY-3D MERSI-II fire spot
 238 products.

239 **3.1 The general principle of fire detection based on MERSI-II**

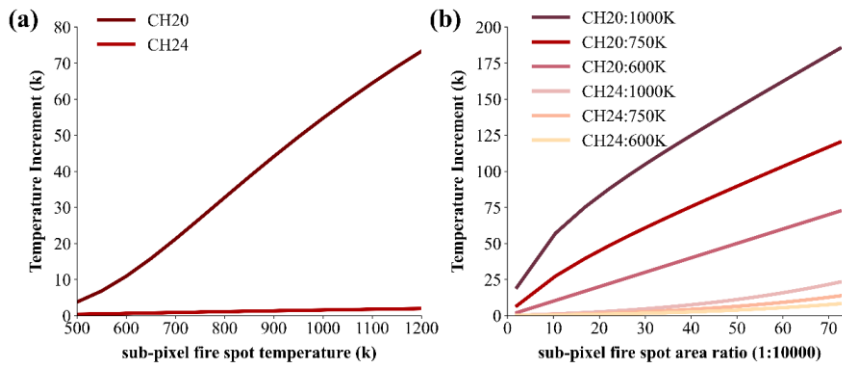
240 Channel 20 of FY-3D MERSI-II is mid-infrared, with a wavelength of 3.55–3.95 μm , while Channels
 241 24 and 25 are far-infrared, with a wavelength of 10.3–11.3 μm and 11.5–12.5 μm , respectively. According
 242 to Wien's displacement law,

243 $\lambda * T = b$, (2)

244 where λ is the peaks at the wavelength, T is the absolute temperature, b is a constant of proportionality
 245 called Wien's displacement constant, equal to about 2898 $\mu\text{m} \cdot \text{K}$. ~~B~~blackbody temperature T is inversely
 246 proportional to peak radiation wavelength λ_{max} , as the higher temperature can lead to the smaller peak

247 radiation wavelength. The peak radiation wavelength of the surface at normal temperature (about 300 K)
 248 is close to that of Channels 24 and 25; the combustion temperature of forest fires is generally 500 K–
 249 1200 K, and the peak wavelength of thermal radiation is close to that of Channel 20. When a fire spot
 250 appears in the observed pixel, the radiance increment in Channel 20 caused by the high temperature in
 251 the small sub-region of the pixel, where the fire spot is located (Since the pixel resolution of the scanning
 252 radiometer is 1.1 km, it is usually not be all open flame areas at the same time in such a large range), is
 253 much higher than surrounding pixels without an open flame and also greater than that in Channels 24
 254 and 25. In this case, the weighted average of radiance increase and brightness temperature increase of
 255 each channel differ notably in this pixel, based on which the fire information can be extracted and
 256 analyzed.

257
 258 As indicated by Fig. 4(a), when the fire spot temperature grows, the brightness temperature of CH20
 259 pixels increases rapidly. Even if the fire spot only accounts for 0.1% the pixel area, the brightness
 260 temperature increment can reach 10 K (44K) when the fire spot is 500 K (900 K). Although the brightness
 261 temperature increase of CH24 also rises with the higher fire spot temperature, it is far lower than that of
 262 CH20. Fig. 4(b) illustrates that as the fire spot area gets larger, the brightness temperature of CH20-
 263 mixed-pixels grows rapidly. It reaches 12K when the fire spot is 900 K, even if the fire spot only accounts
 264 for 0.01% of the pixel area. Similarly, the brightness temperature increment of CH24 grows at a much
 265 lower rate than CH20.



266 **Figure 4** (a): Curves of FY-3D/MERSI-II CH20 and CH24 brightness temperature increment with fire
 267 spot temperature (with fire spot area accounting for 0.1% of pixel area and background temperature at
 268 290 K). (b): Curves of FY-3D/MERSI-II CH20 and CH24 brightness temperature increment with fire
 269 spot area (with fire spot temperature at 600 K, 750 K, and 1000 K, background temperature at 290 K,
 270 and the ratio of fire spot area to pixel area increasing from 0.01% to 0.4%).
 271

272 3.2 Automatic identification algorithms for fire spots

273 3.2.1 Detection of cloud pixels

274 Effective cloud detection is required for generating reliable fire products for the following reasons. Firstly,
 275 the existence of cloud in the atmospheric layers may block the emitted information of fire spots, leading

276 to missed identification. Secondly, specular reflection of cloud can lead to wrong identification of fire
 277 spots. Therefore, cloud identification was conducted before fire identification. Similar to MODIS, FY-
 278 3D also included radiation information from multiple bands and the principle of cloud identification for
 279 FY-3D fire products was similar to that of MODIS. Based on the reflectance difference between cloud
 280 and land pixels, we classified cloud pixels following the rules listed in Table 3.

282 **Table 3** Major rules for cloud pixel ~~determinations~~ identification.

number	conditions
1	$T_{Mir} - T_{far1} < 4K$
2	$T_{Mir} - T_{far1} > 20K$ & $T_{Mir} < 285K$ $T_{far1} < 280K$
3	$R_{vis} > 0.28$ & $SolarZenith < 70^\circ$ $SolarZenith < 60^\circ$ & $SateZenith < 60^\circ$
4	$T_{far1} < 265K$
5	$T_{Mir} < 270K$ & $T_{far1} - T_{far2} < 4K$
6	$T_{far1} < 270K$ & $T_{far1} - T_{far2} > 60K$
7	$T_{Mir} < 320K$ & $T_{Mir} < T_{Mir_TH}$
8	$SolarZenith > 70$ & $R_{vis} > 0.28$ & $T_{Mir} < 320K$

283 T_{Mir} : Mid-infrared channel; T_{far1} : 10.8um Far-infrared channel; T_{far2} : 12um Far-infrared channel; R_{vis} :
 284 Visible light channel; SolarZenith: Solar zenith angle; SateZenith: Satellite zenith angle.

285 Note: These eight rules are set to exclude a diversity of cloud bias. And a pixel that meets any rule
 286 any rule in Table

289 3.2.2 Calculation of background temperature

290 According to the principle of fire spot identification, when a fire spot appears in a pixel (i.e., open flame),
 291 the brightness temperature of the pixel in Channel 20 is significantly higher than the background
 292 brightness temperature (the brightness temperature of surrounding non-fire pixels); the brightness
 293 temperatures of Channels 24 and 25 are also higher than the background, but the temperature difference
 294 is much smaller than Channel 20. In this case, the difference of brightness temperature between fire-spot
 295 pixels and background in both the mid-infrared channel and far-infrared channels can be employed as
 296 important factors for automatic identification of fire spots. Therefore, the background temperature of the
 297 detected pixel is required for identifying fire spots. Since the background temperature cannot be obtained
 298 from the fire-spot pixels, it should be calculated according to the average of their surrounding pixels.
 299 However, the reflection of solar radiation during the daytime also causes a higher brightness temperature
 300 in the mid-infrared channel, which mainly occurs in the zone bare of vegetation, cloud surface, and water
 301 bodies (specular reflection). In particular, the difference of brightness temperature between mid-infrared
 302 and far-infrared channels caused by specular reflection of solar radiation can reach tens of K on the cloud
 303 surface and water bodies. Since the reflection of solar radiation on the bare surface is relatively weak in
 304 the mid-infrared channel, a few degrees of difference can cause non-fire pixels misclassified as fire pixels,

305 due to the high sensitivity requirement for fire identification. When the background brightness
306 temperature is calculated, pixels that already contain fire spots should also be excluded. Therefore,
307 suspected high-temperature pixels, which may already contain fire spot pixels, cloudy pixels, water
308 pixels and those pixels affected by solar flare should be removed for background temperature calculation.

309

310 Furthermore, the pixel size in the mid-infrared channel of a meteorological satellite is about 1 km². Within
311 this range, the underlying surface may be diversified and composed of sub-regions with different
312 fractional vegetation cover (FVC). In the daytime, affected by solar radiation, the brightness temperature
313 of different FVC may vary, making the calculated background temperature higher than expected. To
314 address this issue, Kaufman et al. (1998) suggested the use of standard deviation of background
315 temperature for fire identification, which significantly reduced the overestimation of background
316 temperature caused by different underlying surfaces.

317

318 After above-mentioned disturbing pixels were removed, the average and standard deviation of
319 background temperature in the mid-infrared channel, and the background average and standard deviation
320 of brightness temperature difference between the mid-infrared and far-infrared channels were calculated
321 with peripheral pixels as background pixels.

322

323 The calculation of background temperature was acquired in the following steps. For each 3×3 window,
324 the background temperature is calculated as the mean temperature of all background pixels. Suspicious
325 high-temperature pixels can be identified according to the following conditions:

$$326 \quad T_{Mir} > T_{th} \text{ Or } T_{Mir} > T'_{Mir_bg} + \Delta T_{Mir_bg}$$

327 Where T_{Mir} is the bright temperature in the middle-infrared channel. T_{th} is the threshold for high-
328 temperature pixels in the middle-infrared channel, usually set as sum of the mean bright temperature of
329 all pixels in the window and $2 \times$ its corresponding standard deviation. T'_{Mir_bg} is the mean bright
330 temperature of background pixels.

331

332 ΔT_{Mir_bg} is the allowed difference between the mean background bright temperature and the suspicious
333 high-temperature pixel, usually set as $2.5 \times$ standard deviation of background pixels. If there were less
334 than 20% of pixels were cloudless pixels, then the 3×3 window was extended to $5 \times 5, 7 \times 7, 9 \times 9 \dots 51 \times$
335 51 . If still not applicable, then this pixel was marked as a non-fire pixel.

336 3.2.2 Identification of fire pixels

337 With obtained background temperature, the difference between brightness temperature and background
338 temperature in the mid-infrared channel, as well as the difference of brightness temperature and
339 background temperature between mid-infrared and far-infrared channels, at the candidate pixels could
340 be calculated, based on which we could decide whether the threshold of fire spot identification was
341 reached. If the threshold was reached, the pixel will be preliminarily marked as a fire pixel. Next, for
342 daytime observation data, it is necessary to further check whether the increase of brightness temperature
343 in the mid-infrared channel was interfered by solar radiation in the cloud area. Through the two-stage

344 check, fire pixels could be effectively extracted.

345

346 When the following two conditions are met, a pixel can be identified as fire pixel:

347 (1) $T_{3.9} > T_{3.9bg} + n_1 \times \delta T_{3.9bg}$

348 (2) $\Delta T_{3.9_11} > \Delta T_{3.9bg_11bg} + n_2 \times \delta T_{3.9bg_11bg}$

349 Where T_{39} is the bright temperature of the pixel at 3.9 um. $T_{3.9bg}$ is the background bright temperature.

350 $\delta T_{3.9bg}$ is the standard deviation of bright temperature of background pixels. $\Delta T_{3.9_11}$ is the difference of

351 bright temperature between 3.9 um and 11 um. $\Delta T_{3.9bg_11bg}$ is the difference of background bright

352 temperature between 3.9 um and 11 um. The setting of this condition aimed to identify the difference of

353 land cover types in the window. When the land cover types in the window were generally consistent,

354 $\delta T_{3.9bg_11bg}$ is relatively small. For the identification of fire pixels, when $\delta T_{3.9bg_11bg}$ was smaller than 2k,

355 this value was replaced using 2K. When $\delta T_{3.9bg_11bg}$ was larger than 4k, this value was replaced using 4K.

356 n_1 and n_2 are background coefficients, which varies across regions, observation time and observation

357 angles. For instance, for Northern grasslands, n_1 and n_2 was set as 3 and 3.5, respectively.

358 3.2.3 Identification of noise line

359 Satellite data received by the ground system contain noise. For instance, some scanning lines may contain

360 many noisy pixels that affect fire spot identification. In this case, noise lines, referred to multiple

361 consecutive noisy pixels in one scanning line, should be checked firstly. Since the identification of fire

362 was carried out on the areal map projected with an equal latitude and on the same circle of longitude, the

363 identified latitude and longitude of fire spots failed to reflect the original positions of scanning lines.

364 Therefore, the noise line was identified on the 5-minute data segments before projection. Firstly, the 5-

365 minute data segments were employed to identify fire spots, and the line number of identified fire spot

366 pixels was recorded. Following this, the number of fire spot pixels in each line was counted. When the

367 number of fire spot pixels in a line exceeded the empirical threshold, it was identified as a noise line, and

368 all pixels in the line are marked as noisy ones. In the following process, all pixels in this line were no

369 longer considered for fire-spot identification.

370 3.3 Estimation of fire radiation power (FRP)

371 FRP can be calculated using Stephen–Boltzmann formula (Matson et al., 1984) through the estimation

372 of sub-pixel fire spot area and temperature.

373 3.3.1 Estimation of sub-pixel fire spot area and temperature

374 MERSI-II data is 12 bits, with a quantization level of 0–4095 and high radiation resolution. The spatial

375 resolution is 1.1 km, and the radiance of a pixel observed by the satellite is the weighted average of the

376 radiance of all the ground objects within the pixel range, as

377
$$N_t = (\sum_{i=1}^n \Delta S_i N_{Ti}) / S, \quad (3)$$

378 where N_t is the radiance of the pixel observed by the satellite; t is the brightness temperature

379 corresponding to N_t ; ΔS_i is the area of the i^{th} sub-pixel; N_{Ti} is the radiance of the sub-pixel; T_i is the

380 temperature of the sub-pixel; S is the total area of the pixel.

381
382
383
384
385

Due to different FRP and temperature, underlying surfaces containing fire spots can be divided into fire zones and non-fire zones (background). When fire spots appear, the radiance of pixels containing fire spots (i.e. mixed pixels) can be expressed by the following formula:

$$N_{mix} = P * N_{hi} + (1 - P) * N_{bg} = P * \frac{C_1 V_i^3}{e^{T_{hi}} - 1} + (1 - P) * \frac{C_1 V_i^3}{e^{T_{bg}} - 1}, \quad (4)$$

387 where P is the percentage of sub-pixel fire spot area in the pixel; N_{mix} , N_{hi} , and N_{bg} are the radiance of
388 mixed pixels, sub-pixel fire spot (fire zone) and surrounding background; T_{hi} and T_{bg} are the temperature
389 of sub-pixel fire spots and background; V_i is the central wavenumber of channels; C_1 and C_2 are Planck
390 constants.

391

392 For Eq. (4), there are two unknown variables, P and T_{hi} . According to the characteristics of infrared
393 channels in the scanning radiometer (dynamic brightness temperature and spatial resolution), the
394 radiation increase of high-temperature sources varies notably in different bands. To address this issue, a
395 strategy is employed to estimate the actual area and temperature of fire spots according to the radiation
396 in different infrared channels. When the mid-infrared channel was not saturated, it was used for
397 estimating the sub-pixel fire spot area and temperature. Otherwise, the far-infrared channel was
398 alternatively employed for estimation.

399

400 When a single channel was adopted to estimate the sub-pixel fire spot area, the fire spot temperature was
401 set to an appropriate value, which was 750 K in this product.

402 3.3.2 Calculation of fire radiation power

403 Based on the percentage of sub-pixel fire spot area, P , and fire spot temperature, FRP can be calculated
404 using Stephen–Boltzmann formula:

$$FRP = P * S_{\lambda,\varphi} * \sigma T^4, \quad (5)$$

406 where

407 FRP is fire radiation power, W;

408 $S_{\lambda,\varphi}$ is the sub-pixel fire spot area of pixels located at longitude λ and latitude φ , which is calculated

409 according to the percentage of sub-pixel fire spot area P and the total pixel area;

410 T is the sub-pixel fire spot temperature and set to 750 K;

411 σ is Stephen–Boltzmann constant, 5.6704×10^{-8} (W m⁻² K⁻⁴).

412 3.4 Verification methods

413 Wildfires are characterized by random and rapid changes, so it is difficult to verify the product accuracy
414 of GFR (Global Fire) according to actual ground information. In this paper, the accuracy of FY-3 fire
415 products is tested through visual interpretation and cross-verification of other products. Specifically, due
416 to the extreme large size of GFR datasets, we set the different strategies for accuracy assessment. For
417 visual interpretation, several 5-minute data segments with regional representation were selected for

418 verification using manually identified fire spots; For cross-verification with other fire products, global
419 fire spot data throughout 2019 were employed.

420

421 The error was defined as the distance from the positions (longitude and latitude) of automatically
422 identified fire spot pixels to corresponding manually identified ones. When the difference in latitude and
423 longitude was less than or equal to 0.02° , the automatically identified pixel was regarded as a successful
424 identification.

$$425 \quad \sqrt{(lat1 - lat2)^2 + (long1 - long2)^2} \leq 0.023^\circ$$

426 where $lat1$ and $lat2$ are the latitude of PGS (Product Generation System) fire spot pixels and manually
427 identified pixels (reference pixels); $long1$ and $long2$ are the longitude of PGS fire spot pixels and
428 manually identified pixels (reference pixels), respectively.

429

430 In addition to the visual-check based accuracy assessment at the global scale, we also employed a set of
431 field collected reference data to verify the suitability of FY-3D in China, which is further explained in
432 the following sections.

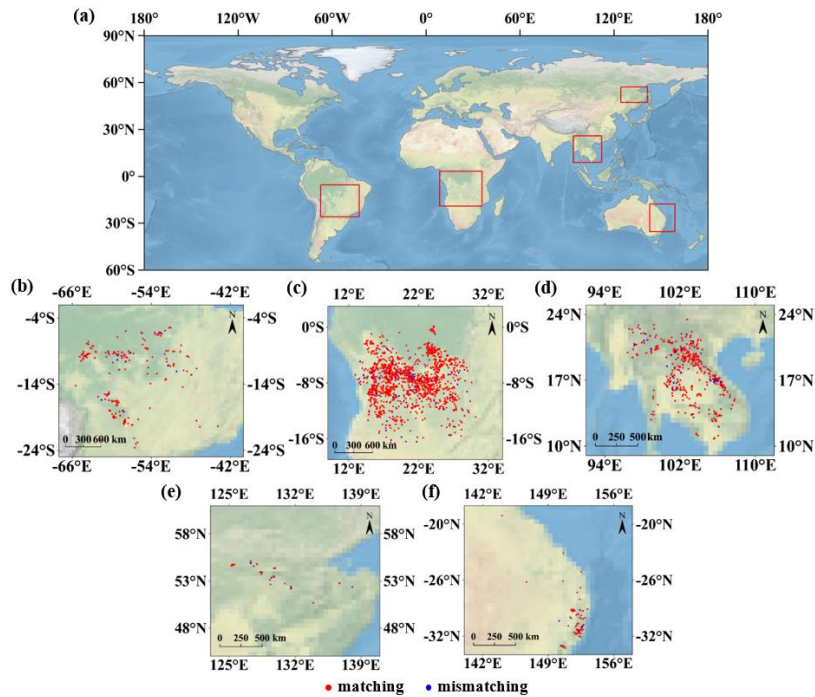
433 4 Results

434 4.1 Global ~~accuracy-scale test~~ assessment of FY-3D fire products based on visual interpretation

435 In this research, 5-minute segments of FY-3D fire products in different continents, including Africa,
436 South America, Indo-China Peninsula, Siberia and Australia were collected at 12:15 (UTC) on June 13,
437 2018, 17: 05 (UTC) on August 21, 2019, 06:15 (UTC) on March 13, 2019, 03:40 (UTC) on November
438 13, 2019, 17:40 (UTC) on May 29, 2018 respectively for visual interpretation. The specific observation
439 positions are shown in Fig. 5 with five corresponding fire detection pictures of FY-3D.

440

441 These regions were selected for evaluating the global reliability of FY-3D fire products for the following
442 reasons. Firstly, Africa, South America, Indo-China Peninsula, Siberia and Australia are the regions with
443 the most frequent fire events across the globe. Secondly, there are rich vegetation in these regions, which
444 provides the foundation for stable combustion across a year. Thirdly, these regions cover large area with
445 generally unified underlying surfaces. Fourthly, these areas are of regional representation: Siberia
446 represents typical regions with frequent forest fires in Northern Hemisphere. Africa represents typical
447 tropical grasslands and forests in the equator regions. South America represents virgin tropical rainforests.



448
 449 **Figure 5** (a), Observation positions from FY-3D MERSI-II. The red frame at the upper right shows FY-
 450 3D MERSI-II is located at the border between Northeast China and Russia. The lower left red frame
 451 shows FY-3D MERSI-II is over east-central South America and the central red frame shows FY-3D
 452 MERSI-II is located in south-central Africa. The middle right red frame shows the FY-3D MERSI-II is
 453 over Indo-China Peninsula and the lower right red frame shows the FY-3D MERSI-II is located in east
 454 Australia. (b)-(f), Fire spot matching diagram between GFR and visual interpretation data of FY-3D
 455 MERSI-II. The red points indicate that GFR matches visual interpretation data, and the blue points
 456 represent that only GFR recognized the fire spots, which was not.

457
 458 Fig. 5 presents the spatial distribution of GFR fire spots and manually identified fire pixels in the 5-
 459 minute segment of the above regions. According to Fig 5b, most fire spots in FY-3D products and
 460 manually extracted fire spots in South America were in same positions. In Fig 5c, most FY-3D
 461 and manually extracted fire spots in Africa coincided or were in a close position. In Fig 5d, despite a few
 462 mismatched fire spots, the position of FY-3D and manually extracted fire spots in Indo-China Peninsula
 463 was consistent. Fig 5e and Fig 5f also show that most fire spots are matched in Russia and Australia.
 464 Table 4 shows accuracy of GFR fire spots in the five typical regions. The accuracy of automatically
 465 identified fire spot in all regions was generally consistent and all exceeded 90%. Since these selected
 466 regions represented distinct vegetation types and located in different hemispheres, the verification of FY-
 467 3D fire products based on 0.24 SMART proved its stability and reliable high-accuracy at the global scale.

468

It is worth mentioning that the visual-check based accuracy assessment mainly considered the commission error, while omission error cannot be effectively revealed for the following reason. The omitted fires were mainly caused by the requirement of minimum burning area. Since the spatial resolution of FY-3D and MODIS active fire products is 1km, small fires (less than 100m²) could not be captured by sensors and recognized through visual check. Meanwhile, the thermal abnormalities at the edge of cloud and water bodies, which could be recognized through visual check. In this case, the visual-check based accuracy assessment mainly considered the commission errors.

Table 4 Verification of fire spot identification based on GFR and SMART Accuracy assessment of FY-3D identified fires based on SMART (Visual check) in different regions:

Region	GFR-based fire spots	Not match with SMART	Coincidence-rate Accuracy (%)
South-central Africa	1429	77	94.6
East-central South America	204	12	94.1
Siberia	32	3	90.6
Australia	85	7	91.8
Indo-China Peninsula	438	32	92.7
Overall	2188	131	94.0

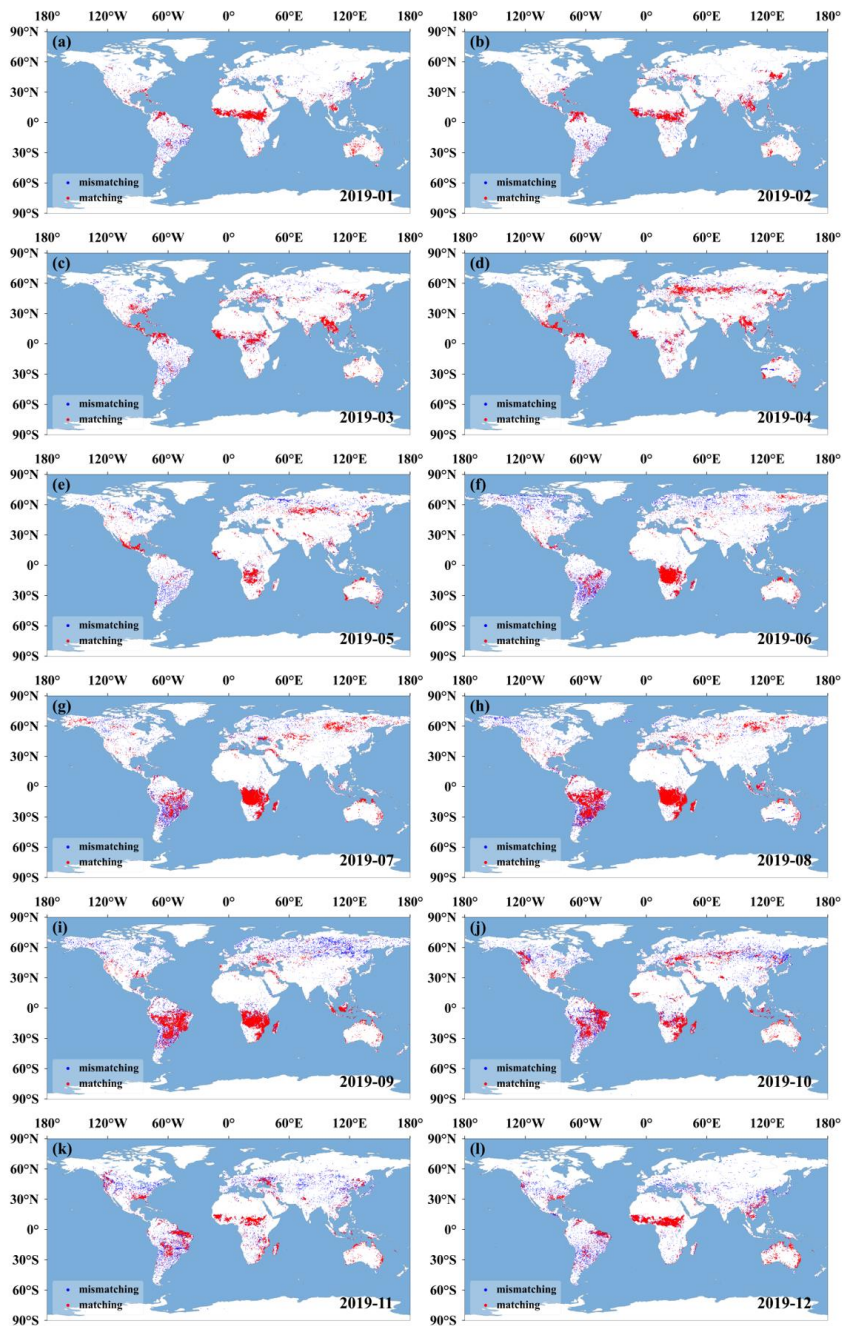
4.2 Cross-verification with between FY-3D and other global fire products MODIS global fire products

The cross-verification between FY-3D fire products and the mainstream MODIS fire products, MYD14A1 V6 (<https://firms.modaps.eosdis.nasa.gov/map/>) with a daily temporal resolution and 1km spatial resolution was conducted using the entire 2019 datasets. The data sets with observation time less than 1 h were selected; the underlying surfaces were visually checked to remove areas covered by non-vegetation such as water, ice and snow, and bare land. According to the criterion that the distance matching between the two fire spot pixels was less than 0.03 °, cross-verification was conducted with different months, underlying surfaces, regions, and fire intensities. In 2019, there were 2,237,714 fire spot pixels in MODIS fire products, 1,866,920 of which were matched with FY-3D fire products, with an overall consistence of 84.4% (as shown in Fig. 6). As shown in Figure 6, global fire spots were mainly distributed in America, south-central Africa, East, and Southeast Asia, Australia, and parts of Europe, and there were notable spatiotemporal variations of identified fire spots. Specifically, given the overall data volume and spatial distribution, the total number of fire spot pixels from MODIS fire products was larger than FY-3D products. For individual regions, the more fire spots, the higher consistence between FY and MODIS fire products. Africa is the region with the most fire spots across the globe. From May to October, a majority of fire spots was located in southern Africa whilst a majority of fire spots from November to next April was located in the middle and western coastal of Africa. The consistence between

带格式的：字体：非加粗

带格式的：两端对齐

498 MODIS and FY-3D products was higher than other regions. The distribution of fire spots in South
499 America also presented seasonal characteristics. From July to October, fire spots mainly concentrated in
500 middle parts of South America. For other seasons, fire spots in South America mainly concentrated in
501 the North and other parts. The consistence between MODIS and FY-3D fire products also demonstrated
502 seasonal differences, with a high consistence from August to November and a relatively low consistence
503 in other seasons. For Eurasia, there were notable seasonal variations of spatial patterns of fire spots.
504 During March to August, there were relatively many fire spots and the consistence between MODIS and
505 FY-3D fire products was relatively high in this region.



506

507 **Figure 6** Spatial distribution difference in global fire spots. The consistence between FY-3D and MODIS
 508 fire products in different months (2019)

509 ~~of 2019.~~

510 In addition to the overall consistence between MODIS and FY-3D fire products, we also conducted cross-
511 verification ~~of between~~ the two global fire products in ~~terms of~~ different months, underlying surfaces,
512 regions and fire intensities as follows.

513 4.2.1 Cross-verification ~~of between~~ MODIS and FY-3D in ~~terms of~~ different months

514 Fig. 7(a) illustrates the monthly ~~precision test of consistence between~~ FY-3D and MODIS fire products
515 in 2019. The ~~consistence~~~~precision~~ in the remaining months is over 80% except that in April, October,
516 and November. The highest appears in July, exceeding 90%, while the lowest is in April, 71%. Detailed
517 parameters can be found in Table 5. From the global perspective, the number of fire spots was larger in
518 July, August and September and the mean consistence between MODIS and FY-3D fire products was
519 larger than 85%. For July when the fire products were the most, the consistence achieved 90%. From
520 January to May, the number of fire spots was relatively small, and the mean consistence was around 80%.
521 The consistence for April was 71%, lowest among all months. The notable monthly variations of the
522 consistence between MODIS and FY-3D fire products was mainly attributed to the uneven spatial
523 distribution of fire spots across the globe. As shown in Fig 6, in June and July, a large number of fire
524 spots mainly concentrated in Africa, South America and Eurasia, leading to a high consistence of fire
525 identification. In April, there were limited and sparsely distributed fire spots in Africa and South America,
526 leading to a low consistence. According to the statistics, the number of fire spots was positively correlated
527 with the consistence between different fire products. Meanwhile, in seasons when fire could last longer,
528 the consistence was relatively higher.

529 **Table 5** Cross-satellite comparison between FY-3D and MODIS fire products.

Time	Match	Mismatch	Total	Consistence (%)
201901	70799	14188	84987	83
201902	66849	14717	81566	82
201903	105176	22576	127752	82
201904	94474	39250	133724	71
201905	75703	17135	92838	82
201906	174587	33862	208449	84
201907	362108	39683	401791	90
201908	315182	51627	366809	86
201909	226363	47607	273970	83
201910	115975	33956	149931	77
201911	102240	27732	129972	79
201912	157464	28461	185925	85
Total	1866920	370794	2237714	83.4

530 **4.2.2 Cross-verification between of MODIS and FY-3D on in terms of different underlying surfaces**

531 Statistical analysis of consistenceprecision is carried out with different types of underlying surfaces. The
 532 data of underlying surfaces is the global land use are detailed in Table 6.

533
 534 The 15 types of underlying surfaces were selected for verification. Table 6 and Fig. 7(c) shows the
 535 consistence of FY-3D and MODIS fire products with different underlying surfaces. From the
 536 classification of different underlying surfaces, the remaining types are over 80% except (11) Post-
 537 flooding or irrigated croplands (or aquatic), (14) Rainfed crops, (20) Mosaic cropland (50-70%) /
 538 vegetation (grassland/shrubland/forest) (20-50%), (140) Closed to open (>15%) herbaceous vegetation
 539 (grassland, savannas or lichens/mosses), and (150) Sparse (<15%) vegetation. When the underlying
 540 surface is the open (15%–40%) coniferous and deciduous forest or evergreen forest, the
 541 consistenceprecision is the highest, at 93%. In addition, according to the classification of underlying
 542 surfaces, the fire spot identification shows high consistenceprecision when the underlying surface is the
 543 forest. The consistence between FY-3D and MODIS fire spots on different underlying surfaces in each
 544 month was demonstrated in Table 7. Clearly, we can found the fluctuation of consistence across seasons
 545 due to the variation of combustible vegetation, which influenced the detecting capability of MODIS and
 546 FY-3D.

547
 548 The low consistence between FY-3D and MODIS fire products was observed for underlying surface 11,
 549 14, 20, 140 and 150. Specifically, 11, 14 and 20 could be categorized as farmlands. 140 was mainly
 550 occupied by herbaceous vegetation or sparse grasslands. 150 was mainly occupied by sparse grasslands.
 551 Generally, these surfaces were all covered by sparse or unstable vegetation, the fire on which can last for
 552 a relatively short period. Meanwhile, the observation time lag between FY-3D and MODIS was larger
 553 than 30 minutes. Therefore, the consistence of FY-3D and MODIS fire products on these surface types
 554 was lower than other surface types.

555 **Table 6** Classification of underlying surfaces (land cover types).

带格式的：居中

ID	Definition of underlying surfaces
11	Post-flooding or irrigated croplands (or aquatic)
14	Rainfed croplands
20	Mosaic cropland (50-70%) / vegetation (grassland/shrubland/forest) (20-50%)
30	Mosaic vegetation (grassland/shrubland/forest) (50-70%) / cropland (20-50%)
40	Closed to open (>15%) broadleaved evergreen or semi-deciduous forest (>5m)
50	Closed (>40%) broadleaved deciduous forest (>5m)
60	Open (15-40%) broadleaved deciduous forest/woodland (>5m)
70	Closed (>40%) needleleaved evergreen forest (>5m)
90	Open (15-40%) needleleaved deciduous or evergreen forest (>5m)
100	Closed to open (>15%) mixed broadleaved and needleleaved forest (>5m)
110	Mosaic forest or shrubland (50-70%) / grassland (20-50%)
120	Mosaic grassland (50-70%) / forest or shrubland (20-50%)
130	Closed to open (>15%) (broadleaved or needleleaved, evergreen or deciduous) shrubland

	(<5m)
140	Closed to open (>15%) herbaceous vegetation (grassland, savannas or lichens/mosses)
150	Sparse (<15%) vegetation

556

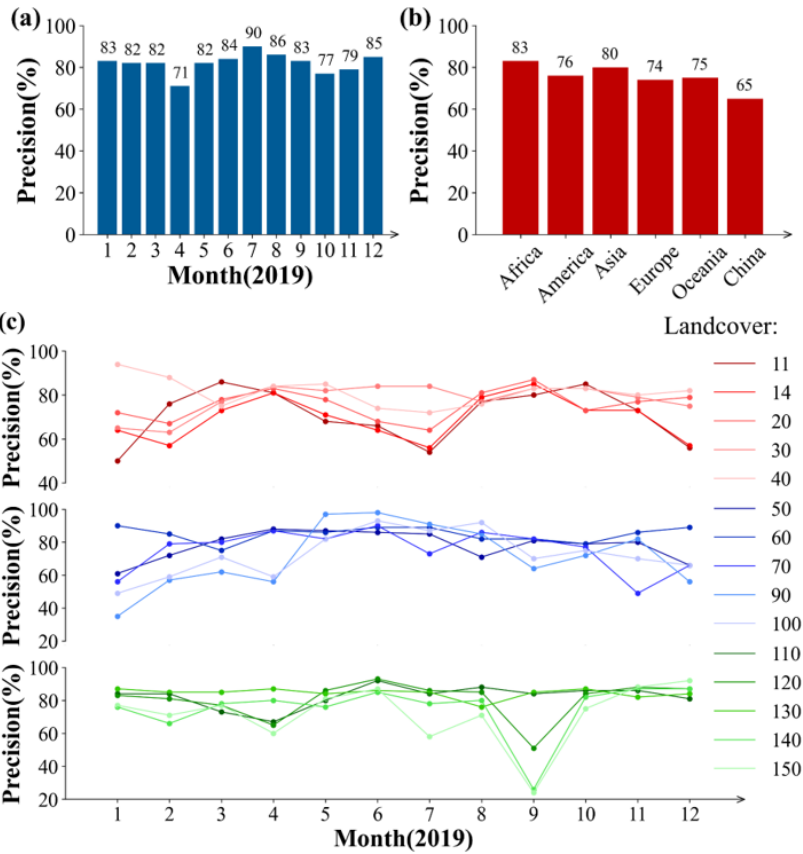
557 **Table 7** the consistence between FY-3D and MODIS fire spots on different underlying surfaces in each month (total FY-3D pixels (~~matched percentage~~ consistence)).

ID	Jan	Feb	Mar	Apr	May	Jun	Jul	Aug	Sep	Oct	Nov	Dec
11	754 (50%)	1471(76%)	1651(86%)	450(81%)	201(68%)	344(66%)	353(54%)	678(77%)	1786(80%)	1516(85%)	558(73%)	416(56%)
14	4459(64%)	5024(57%)	7745(73%)	11439(81%)	6818(71%)	4137(64%)	2135(56%)	4122(79%)	8090(85%)	4561(73%)	3154(73%)	1663(57%)
20	8033(72%)	8596(67%)	13513(78%)	20282(83%)	14772(78%)	5216(68%)	2921(64%)	5449(81%)	11970(87%)	5858(73%)	4721(77%)	5572(79%)
30	5786(65%)	7227(63%)	13018(77%)	22626(84%)	26523(82%)	23024(84%)	16007(84%)	6455(77%)	14534(83%)	16523(83%)	8646(79%)	5199(75%)
40	45313(94%)	38194(88%)	25315(75%)	63474(84%)	69987(85%)	14770(74%)	8265(72%)	7107(76%)	22921(83%)	31839(83%)	14646(80%)	9556(82%)
50	3454(61%)	8398(72%)	19960(82%)	45387(88%)	51148(87%)	42981(86%)	25424(85%)	4356(71%)	5481(81%)	6237(79%)	3713(80%)	1920(66%)
60	36987(90%)	6321(85%)	5570(75%)	25021(87%)	49083(86%)	74660(89%)	59345(89%)	6526(82%)	3028(82%)	4478(79%)	12513(86%)	18192(89%)
70	1863(56%)	3655(79%)	5031(80%)	4052(87%)	1865(82%)	3411(90%)	2123(73%)	3402(86%)	2346(82%)	2791(77%)	704(49%)	719(66%)
90	840(35%)	3255(57%)	8901(62%)	11125(56%)	61299(97%)	135344(98%)	32767(91%)	18539(85%)	4645(64%)	4076(72%)	1484(82%)	608(56%)
100	1079(49%)	1851(59%)	3423(71%)	1988(59%)	2444(82%)	6027(93%)	3677(87%)	8695(92%)	2813(70%)	2596(75%)	565(70%)	397(66%)
110	19896(84%)	13825(84%)	4194(73%)	3669(67%)	6504(80%)	11351(92%)	7407(84%)	7223(88%)	4268(84%)	4983(86%)	5009(86%)	5409(81%)
120	6568(83%)	3406(81%)	3639(77%)	3602(65%)	9037(86%)	12972(93%)	7122(86%)	4999(85%)	3574(51%)	2379(84%)	4651(88%)	4710(87%)
130	38258(87%)	18784(85%)	19935(85%)	34627(87%)	37668(84%)	34189(86%)	20881(85%)	6963(76%)	20071(85%)	27134(87%)	8320(82%)	15465(84%)
140	3941(76%)	2905(66%)	6159(78%)	7692(80%)	6756(76%)	8964(85%)	5139(78%)	3104(80%)	13060(26%)	3562(82%)	3844(87%)	4270(87%)
150	5760(77%)	5073(71%)	8872(77%)	7268(60%)	15938(81%)	19370(87%)	10467(58%)	4106(71%)	12991(24%)	3532(75%)	6359(88%)	8994(92%)

4.2.3 Cross-verification of between MODIS and FY-3D in terms of different regions

The global monitoring area is divided into Africa, America, Asia, Europe, and Oceania. The verification demonstrates the results with the highest consistenceprecision (over 80%) are found in Africa and Asia, and those in America, Europe, and Oceania show the consistenceprecision over 70%. The FY-3D/MERSI-II fire identification algorithm draws lessons from the MODIS algorithm and has been improved on that basis, and targeted development has been made for the underlying surface and climatic conditions in China, so it is necessary to test the matching results in China separately. It shows that China's regional consistency of results in China is lower than other continents, only 65%. Compared with other continents, the low consistence between FY-3D and MODIS fire products in China may be attributed to the following reason. Thanks to the field-collected data, the algorithm for fire detection using FY-3D specifically included the underlying surfaces and surrounding geographical conditions in China. Therefore, FY-3D has the potential to provide more reliable fire products for China.

According to the feedback on practical application in China, especially during the period from July to September, when there were much precipitation, cloud cover, there should be limited fire spots identified. However, based on MODIS fire products, there were many fire spots during this period, which were much more than FY-3D detected fire spots. The consistence between MODIS and FY-3D fire products in China was only 65%. To further examined the suitability of FY-3D fire products in China, the accuracy assessment of FY-3D and MODIS fire products was conducted based on ground truth data and explained in the following sections. Specifically, the fire spot precision of FY-3D/MERI-II was higher than 85%, which indicated that the precision of the MODIS algorithm is inferior to FY-3D/MERI-II in China with the decline in instrument performance (see Fig. 7(b) for details).



581
582
583
584
585
586
587

Figure 7 Consistency between FY-3D and MODIS fire products under different conditions. (a)-(c). (a): Monthly precision test of fire spots identified by FY-3D and MODIS fire products in different months. (b): Consistency between FY-3D and MODIS fire products in different regions. (c): Consistency between FY-3D and MODIS fire products in different underlying surfaces.

带格式的: 字体: 非加粗
带格式的: 居中

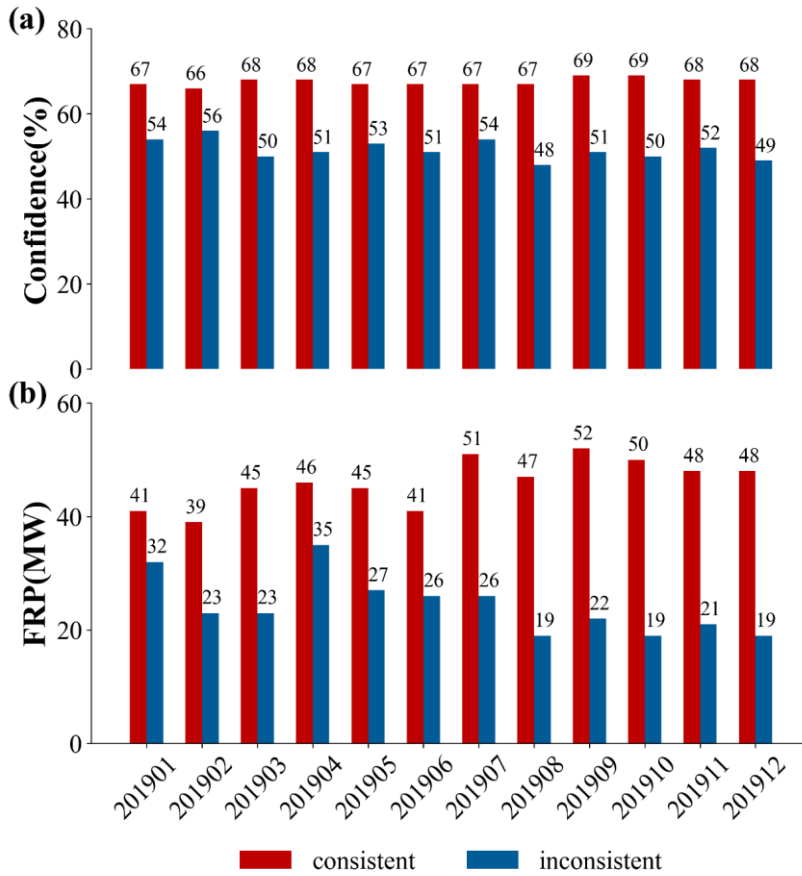
588 **4.2.4 Cross-verification of MODIS and FY-3D in terms of fire intensities**

589 The confidence of fire spots and the fire intensity represented by FRP are analyzed respectively, and the
590 data comes from the MODIS fire spot list. Fig. 8(a) and Fig. 8(b) are statistical diagrams of confidence
591 and FRP, respectively. From Fig. 8(a), the confidence of the matched pixels of the two satellites is above
592 66%, while that of the mismatched ones is less than 60% and even lower than 50% in some months. In
593 other words, the higher confidence indicates the higher matching degree. As indicated by Fig. 8(b), the
594 FRP of the matched pixels of two satellites is mostly above 40 MW, while that of the unmatched pixels
595 is less than 40 MW and even lower than 20 MW in some months. Accordingly, the greater fire intensity

596 leads to the greater probability of simultaneous observation by the two satellites and the higher matching
 597 degree between their results.

598

599 Two major findings were identified based on the comparison between FY-3D and MODIS fire products
 600 in terms of fire intensity: Firstly, the higher the credential of the identified fire, the higher consistence
 601 between FY-3D and MODIS fire products. When the credential was larger than 65%, both FY-3D and
 602 MODIS could effectively identify the candidate pixel as fire pixel. In other words, the parameter of
 603 credential in MODIS fire product provides important reference for fire detection. Secondly, FRP is an
 604 index for the heat radiation of the fire. The larger FRP, the larger consistence between FY-3D and MODIS
 605 was, indicating a higher accuracy of fire detection. Therefore, the difficulty for fire detection mainly lies
 606 in the detection of weak fires.

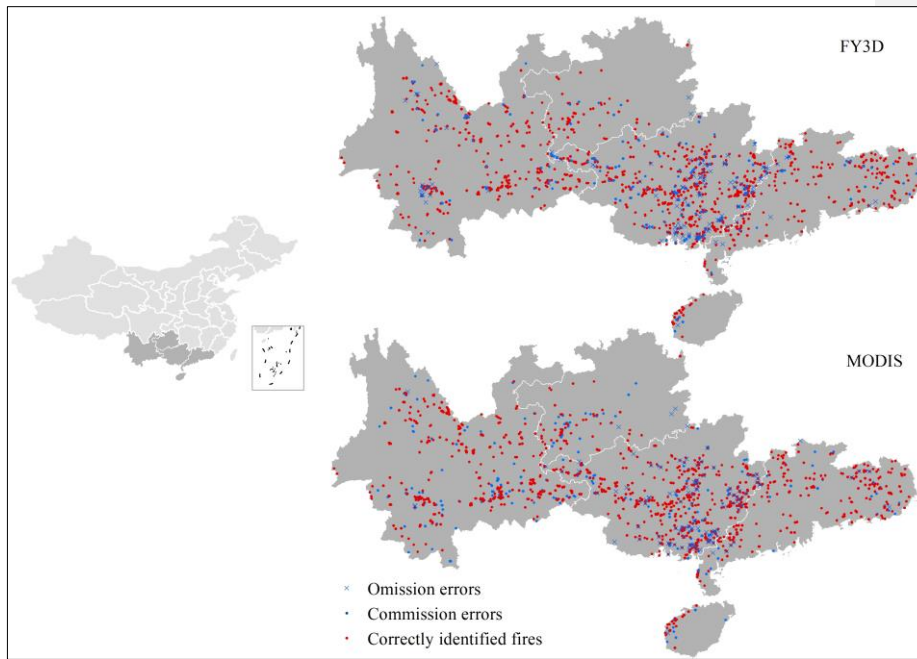


607

608 **Figure 8** (a)-(b). (a):Relationship between matching and confidence of different fire spots: Confidence of
 609 consistent and inconsistent pixels between FY-3D and MODIS fire products (b): FRP of consistent and
 610 inconsistent pixels between FY-3D and MODIS fire products Relationship between matching and FRP
 611 of different fire spots.

612 **4.3 Accuracy assessment of FY-3D fire products in China based on field collected reference**

613
614
615
616 In addition to visual-check and consistence check, we also referred to a large-scale field experiment to
617 comprehensively assess the suitability of FY-3D fire products in China. STATE GRID Corporation of
618 China and China Meteorological Administration jointly conducted a fire-detection experiment
619 throughout 2020 in five provinces Guangdong, Guangxi, Yunnan, Guizhou and Hainan in China. This
620 experiment was conducted in the following steps. A large number of drones were employed to check the
621 occurrence of fires. According to the local passing time of FY-3D, these drones reported the coordinate
622 of actual fires for verifying the accuracy of FY-3D identified fires. The temporal difference between
623 passing time of FY-3D and reported time was controlled within 1 hour. In this case, both omitted and
624 misidentified fires could be effectively recognized (As shown in Figure 9). Based on the field collected
625 reference of fires, we evaluated the suitability of FY-3D fire products in China (Table 8).



626
627 **Fig 9 Accuracy assessment of FY-3D fire products in China based ground-based reference**

628
629 **Table 8 Accuracy assessment based on field ground truth**

	Correct	Omission	Commission	Accuracy (%)	Accuracy without
	Identification				omission(%)
FY-3D	1178	133	172	79.43%	88.50%
MODIS	1201	112	306	74.23%	79.69%

带格式的: 行距: 单倍行距

带格式的: 字体: 加粗

带格式的: 字体: 加粗

带格式的: 字体: 非加粗

带格式的: 居中

带格式的: 字体: 加粗

带格式的: 字体: 加粗

带格式表格

带格式的: 字体: 加粗

带格式的: 居中

带格式的: 字体: 加粗

带格式的: 居中

带格式的: 字体: 非加粗

631 As shown in Figure 9 and Table 8, FY-3D products achieved a good accuracy of 79.43% in China.
632 Meanwhile, MODIS also achieved a good accuracy of 74.23%. As introduced above, the omission error
633 of FY-3D and MODIS fire products was mainly attributed to small fire area, which failed to meet the
634 minimum fire area recognizable by sensors. When simply considering the commission error, FY-3D fire
635 products achieved an accuracy of 88.50%, notably higher than that of MODIS (79.69%). This result
636 proved that with the consideration of local underlying surfaces, FY-3D fire products are more suitable
637 for fire monitoring in China.

638 **5 Discussion**

639 **5.1 Advantages, limitations and implementations of FY-3D fire products**

640 As satellite instruments keep aging in the harsh space environment, the degradation of sensors is
641 inevitable (Tian et al., 2015). Theoretically, sensor degradation can be corrected through atmospheric
642 calibration. However, during the mission life, the solar diffuser and stability monitor required for
643 atmospheric calibration also change across time (Wang et al., 2012). Since the MODIS instrument has
644 been working for ~~more than~~nearly 20 years, its performance for fire detection ~~degrades notably will, if~~
645 not already, degrade in the future. Furthermore, similar to VIIRS and other algorithms, MODIS fire
646 products may have large uncertainties in such regions as China (Fu et al., 2020; Ying et al., 2019).

647
648 As one major product of the FY-3D meteorological satellite, FY-3D fire products ~~boasts~~ boasts the ~~highest~~
649 resolution and ~~accuracy~~precision in China by specifically including the underlying surface parameters
650 collected in China. Compared with MODIS and VIIRS, MERSI- II shows the resolution of 250 m in the
651 far-infrared channel, which is the highest among meteorological satellites of the same type. The FY-3D
652 fire identification algorithm learns from the advantages and technical ideas of MODIS and VIIRS fire-
653 identification algorithms. Furthermore, FY-3D fire products have been optimized in terms of auxiliary
654 parameters, fire identification, and re-identification as follows:

655
656 **Auxiliary parameters:** Since the sole use of vegetation index is limited to reflect combustible materials,
657 climatic boundaries and geographical environment data, which ~~had~~have a strong influence on vegetation
658 types and growth, ~~were~~are added to FY-3D fire identification.

659
660 **Fire identification:** FY-3D adopts the adaptive threshold and reduces the limitations caused by fixed
661 thresholds of MODIS and VIIRS algorithms. Meanwhile, FY employs a re-identification index according
662 to geographical latitude, underlying surface types, as well as the influence by cloud, water bodies and
663 bare land, —and the comprehensive consideration of multiple influencing factors increases the accuracy
664 of fire identification; Thirdly, since the far-infrared channel plays an important role in fire identification
665 and FY-3D has a high resolution of 250 m in the far-infrared channel, ~~The~~the ~~precision~~accuracy of fire
666 identification is improved.

667
668 **Fire re-identification:** FY-3D fire products can be used for both global climate change research and such

669 practical implementations as forest and grassland fire prevention with a higher requirement for
670 ~~precision~~accuracy. Based on the initially identified fire spots, FY-3D employed the re-identification
671 index to further remove ~~false~~ fire spots at cloud edges, ~~cloud gaps~~, water body edges, and ~~conventional~~
672 ~~heat sources and on bare land and other~~ high-ly-reflection~~ve~~ underlying surfaces.

673
674 MODIS fire product is one of the most significant and frequently employed fire products with mature
675 algorithms. Compared with MODIS, FY-3D receives limited emphasis for its capability of fire
676 monitoring, which is mainly attributed to its short service periods. On one hand, due to its long time
677 series and general reliability, MODIS fire products remained a major choice for monitoring long-term
678 variations of fire spots across the world. However, the ~~long-term running continuous degradation of~~
679 MODIS sensors led to ~~the growing large~~ uncertainties to the quality of recent and future MODIS fire
680 products. In this case, thanks to its similar spatio-temporal resolution ~~and~~, high ~~consistence and less than-~~
681 ~~th difference of visiting time~~precision, FY-3D fire products ~~s~~ ~~haves~~ the potential to be widely employed
682 as the ~~potential alternative replacement~~ and continuity of global MODIS fire products. Meanwhile, FY-
683 3D fire products have a higher reliability in China and its surrounding regions than other fire products.
684 Therefore, FY-3D fire products are an ideal selection for fire monitoring ~~in across~~ China.

685
686 The main implementation of FY-3D fire products is fire monitoring. For vast forest and grassland areas,
687 it is inefficient and time-consuming for manual and aircraft patrol to monitor wildfires. Satellite remote
688 sensing can work for continuous space with a wide monitoring range, providing massive information in
689 fire detection, disaster relief, and post-disaster assessment.

690
691 In addition to the fire spot identification and real-time fire tracking, the impact of pollutants produced by
692 biomass combustion on the environment is another important topic. In China and Southeast Asia, air
693 pollution caused by biomass burning has been intensified in recent years. Agricultural activities such as
694 crop-residue burning and wildfires (e.g. forest fires and grassland fires) emit airborne pollutants (e.g.
695 PM_{2.5}, PM₁₀, CO). In this regard, FY-3D fire products can be used as the emission sources for estimating
696 its environmental effects.

697 **5.2 Future extension of FY-3D fire products**

698 China has just launched FY-3E and FY-4B satellites in June and July, 2021. Amid the launch and
699 operation of a new generation of Fengyun meteorological satellites, the accuracy and timeliness of fire
700 monitoring by meteorological satellites have been largely enhanced. Thanks to the improved
701 meteorological data, which provides useful reference to understand the current status of combustibles
702 and potential fire risk, FY-3D satellite will be taken as a better data source to produce various secondary
703 products for fire monitoring and prediction. Based on traditional fire spot identification, further research
704 should concentrate on the assessment of fire area, estimation of biomass carbon emission, prediction of
705 smoke impact, and early warning of forest and grassland fire using the series of Fengyun meteorological
706 satellites. For instance, the water content of combustibles is closely related to temperature, light, and
707 cloud cover, which is an important indicator in forest and grassland fire forecasts. However, this variable

708 was rarely considered in previous fire products. Based on ~~the a~~ series of products ~~of from~~ Fengyun
709 meteorological satellites, such as surface temperature, vegetation index, surface evapotranspiration, solar
710 radiance, and cloud cover, FY-3D fire products can be improved by establishing an estimation model for
711 the water content of combustibles. Meanwhile, with the fire products such as fire spot and smoke, and
712 the meteorological products such as wind field data from Fengyun series satellites, we can predict the
713 impact of smoke caused by forest and grassland fires on the atmospheric environment in the surrounding
714 ~~and even remote~~ areas. In the future implementations, Fengyun meteorological satellites will play a
715 greater role in monitoring, early warning, and forecast-~~ofing~~ global fires and their ecological impacts.
716

717 6 Data availability

718 The MYD14A1 Version 6 is available via the NASA FIRMS portal
719 (<https://firms.modaps.eosdis.nasa.gov/map/>, NASA FIRMS, 2021). FY-3D fire products are now
720 downloadable from our official website (<http://satellite.nsmc.org.cn/portalsite/default.aspx>, NSMC, 2021)
721 using registered account and password. For the convenience of data check and trial experiments, a test
722 account is provided as
723 Account: 1256931756@qq.com
724 Password: yangjing1211

725 7 Conclusions

726 With a similar spatial and temporal resolution, we produced FY-3D global fire products, aiming to serve
727 as the ~~potential alternative and continuity-and-replacement~~ for MODIS fire products, ~~which has been~~
728 ~~degrading after long term service~~. The sensor parameters and major algorithms for noise detection and
729 fire identification in FY-3D products were introduced. For ~~visual-check-based~~ accuracy assessment, five
730 typical regions, Africa, South America, Indo-China Peninsula, Siberia and Australia, across the globe
731 were selected and the overall ~~consistence between FY-3D fire products and reference data~~ accuracy
732 exceeded 94%, ~~with a more than 90% consistence in all regions~~. We also compared the FY-3D and
733 MODIS fire products for their consistence. The result suggested that the overall consistence was 84.4%,
734 with a fluctuation across seasons, surface types and regions. The high accuracy and consistence with
735 MODIS products proved that FY-3D fire product was an ideal tool for global fire monitoring. Based on
736 field-collected reference data, we further evaluated the suitability of FY-3D fire products in China. The
737 overall accuracy and accuracy (without considering omission errors) was 79.43% and 88.50%
738 respectively, higher than that of MODIS fire products. ~~Specially~~, since detailed geographical conditions
739 in China were considered, FY-3D products should be preferably employed for monitoring fires and
740 estimating its environment effects in China.

741 Author contributions

742 J. C., W.Z and C,L produced FY-3D global fire products and the official website. J.C., Z.C., B. G., M, L.
743 conceived the manuscript. J.C., C.Z., Q, Y., M.X., X.C., and J, Y. conducted data analysis and produced
744 Figures. J.C and Z.C wrote the draft. Z.C and M,L. reviewed and revised the manuscript.

745 Competing interests

746 The authors have no competing interests.

747 Financial support

748 This work was supported by the National Natural Science Foundation of China (Grant No.42171399)
749 and National Key R&D Program of China (2021YFC3000300).

750 **References**

- 751 [Abram, N.J., Henlev, B.J. and Sen Gupta, A.: Connections of climate change and variability to large and](#)
752 [extreme forest fires in southeast Australia, *Commun. Earth Environ.*, 2, 8,](#)
753 <https://doi.org/10.1038/s43247-020-00065-8>, 2021.
- 754 [Alisjahbana, A.S. and Busch, J.M.: Forestry, Forest Fires, and Climate Change in Indonesia. *Bull. of*](#)
755 [Indones. Econ. Stud.](#), 53, 111–136, <https://doi.org/10.1080/00074918.2017.1365404>, 2017.
- 756 [Andela, N., Morton, D.C., Giglio, L., Paugam, R., Chen, Y., Hantson, S., van der Werf, G. R., and](#)
757 [Randerson, J.T.: The Global Fire Atlas of individual fire size, duration, speed and direction, *Earth Syst.*](#)
758 [Sci. Data](#), 11, 529–552, <https://doi.org/10.5194/essd-11-529-2019>, 2019.
- 759 [Barnes, B.B., Cannizzaro, J.P., English, D.C., and Hu, C.: Validation of VIIRS and MODIS reflectance](#)
760 [data in coastal and oceanic waters: An assessment of methods, *Remote Sens. Environ.*, 220, 110-123,](#)
761 <https://doi.org/10.1016/j.rse.2018.10.034>, 2019.
- 762 [Boles, S.H. and Verbyla, D.L.: Comparison of three AVHRR-based fire detection algorithms for interior](#)
763 [Alaska, *Remote Sens. Environ.*, 72, 1-16, https://doi.org/10.1016/S0034-4257\(99\)00079-6](#), 2000.
- 764 [Cerdeira, Lloret, F., Ruiz, J.E., and Vandermeer, J.H.: Tree mortality following ENSO-associated fires and](#)
765 [drought in lowland rain forests of Eastern Nicaragua, *For. Ecol. Manage.*, 265, 248-257,](#)
766 <https://doi.org/10.1016/j.foreco.2011.10.034>, 2012.
- 767 [Cochrane, M.: Fire science for rainforests, *Nature*, 421, 913-919, <https://doi.org/10.1038/nature01437>,](#)
768 [2003.](#)
- 769 [Doelling, D.R., Wu, A., Xiong, X., Scarino, B.R., Bhatt, R., Haney, C.O., Morstad, D., and Gopalan, A.:](#)
770 [The radiometric stability and scaling of collection 6 Terra-and Aqua-MODIS VIS, NIR, and SWIR](#)
771 [spectral bands, *IEEE Trans. Geosci. Remote Sensing*, 53, 4520-4535,](#)
772 <https://doi.org/10.1109/TGRS.2015.2400928>, 2015.
- 773 [Dozier, J.: A method for satellite identification of surface temperature fields of subpixel resolution,](#)
774 [Remote Sens. Environ.](#), 74, 33-38, [https://doi.org/10.1016/0034-4257\(81\)90021-3](https://doi.org/10.1016/0034-4257(81)90021-3), 1981.
- 775 [Fang, H., Wei, S., and Liang, S.: Validation of MODIS and CYCLOPES LAI products using global field](#)
776 [measurement data, *Remote Sens. Environ.*, 119, 43-54, <https://doi.org/10.1016/j.rse.2011.12.006>, 2012.](#)
- 777 [Fensholt, R., and Proud, S.R.: Evaluation of earth observation based global long term vegetation trends—](#)
778 [Comparing GIMMS and MODIS global NDVI time series, *Remote Sens. Environ.*, 119, 131-147,](#)
779 <https://doi.org/10.1016/j.rse.2011.12.015>, 2012.
- 780 [Flannigan, M.D. and Haar, T.H.: Forest fire monitoring using NOAA satellite AVHRR, *Can. J. For. Res.*,](#)
781 [16, 975-982, <https://doi.org/10.1139/x86-171>, 1986.](#)
- 782 [Giglio, L., Boschetti, L., Roy, D.P., Humber, M.L., and Justice, C.O.: The Collection 6 MODIS burned](#)
783 [area mapping algorithm and product, *Remote Sens. Environ.*, 217, 72-85,](#)
784 <https://doi.org/10.1016/j.rse.2018.08.005>, 2018.

带格式的: 段落间距段前: 0.5 行, 不允许文字在单词中间换行

785 [Guo, J., Zhang, X., Cao, C., Che, H., Liu, H., Gupta, P., Zhang, H., Xu, M., and Li, X.: Monitoring haze](#)
786 [episodes over the Yellow Sea by combining multisensor measurements, *Int. J. Remote Sens.*, 31, 4743-](#)
787 [4755, <https://doi.org/10.1080/01431161.2010.485213>, 2010.](#)

788 [Guo, L., Ma, Y., Tigabu, M., Guo, X., Zheng, W., and Guo, F.: Emission of atmospheric pollutants during](#)
789 [forest fire in boreal region of China, *Environ. Pollut.*, 264, 114709,](#)
790 [https://doi.org/10.1016/j.envpol.2020.114709, 2020.](#)

791 [Hall, J.V., Zhang, R., Schroeder, W., Huang, C., and Giglio, L.: Validation of GOES-16 ABI and MSG](#)
792 [SEVIRI active fire products, *Int. J. Appl. Earth Obs. Geoinf.*, 83, 101928,](#)
793 [https://doi.org/10.1016/j.jag.2019.101928, 2019.](#)

794 [Huff, A.K., Kondragunta, S., Zhang, H., and Hoff, R.M.: Monitoring the impacts of wildfires on forest](#)
795 [ecosystems and public health in the exo-urban environment using high-resolution satellite aerosol](#)
796 [products from the visible infrared imaging radio-meter suite \(VIIRS\), *Environ. Health Insights*, 9s2,](#)
797 [EHI.S19590, <https://doi.org/10.4137/ehi.s19590>, 2015.](#)

798 [Jacobson, M.Z.: Effects of biomass burning on climate, accounting for heat and moisture fluxes, black](#)
799 [and brown carbon, and cloud absorption effects, *J. Geophys. Res. Atmos.*, 119, 2014JD021861,](#)
800 [https://doi.org/10.1002/2014JD021861, 2014.](#)

801 [Jethva, H., Torres, O., and Field, R.D.: Connecting Crop Productivity, Residue Fires, and Air Quality](#)
802 [over Northern India, *Sci. Rep.*, 9, 16594, <https://doi.org/10.1038/s41598-019-52799-x>, 2019.](#)

803 [Johnston, F.H., Henderson, S.B., Chen, Y., Randerson, J.T., Marlier, M., DeFries, R.S., Kinney, P.,](#)
804 [Bowman, D.M., and Brauer, M.: Estimated global mortality attributable to smoke from landscape fires,](#)
805 [Environ. Health Perspect, 120, <https://doi.org/10.1289/ehp.1104422>, 2012.](#)

806 [Kaufman, Y.J., Kleidman, R.G., and King, M.D.: SCAR - B fires in the tropics: properties and remote](#)
807 [sensing from EOS-MODIS, *J. Geophys. Res.-Atmos.*, 103\(D24\): 31955-31968,](#)
808 [https://doi.org/10.1029/98JD02460, 1998.](#)

809 [Kaufman, Y.J., Setzer, A., and Justice, C.: Remote Sensing of Biomass Burning in the Tropics, *Fire in*](#)
810 [the Tropical Biota, 84, 371-399, \[https://doi.org/10.1007/978-3-642-75395-4_16\]\(https://doi.org/10.1007/978-3-642-75395-4_16\), 1990.](#)

811 [Keegan, K.M., Albert, M.R., McConnell, J.R., and Baker, I.: Climate change and forest fires](#)
812 [synergistically drive widespread melt events of the Greenland Ice Sheet, *Proc. Natl. Acad. Sci. U.S.A.*,](#)
813 [111, 7964–7967, <https://doi.org/10.1073/pnas.1405397111>, 2014.](#)

814 [Keeley, J.E., Bond, W.J., Bradstock, R.A., Pausas, J.G., and Rundel, P.W.: Fire in Mediterranean](#)
815 [ecosystems: Ecology, evolution and management, Cambridge University Press, Cambridge, United](#)
816 [Kingdom, 2011.](#)

817 [Kelly, L.T., Giljohann, K.M., Duane, A., Aquilu é N., Archibald, S., and Battlori, E.: Fire and biodiversity](#)
818 [in the Anthropocene, *Science*, 370, eabb0355, <https://doi.org/10.1126/science.abb0355>, 2020.](#)

819 [Li, F., Zhang, X., Kondragunta, S., and Lu, X.: An evaluation of advanced baseline imager fire radiative](#)
820 [power based wildfire emissions using carbon monoxide observed by the Tropospheric Monitoring](#)

821 [Instrument across the conterminous United States, Environ. Res. Lett., 15, 094049,](#)
822 <https://doi.org/10.1088/1748-9326/ab9d3a>, 2020.

823 [Li, J., Bo, Y., and Xie, S.: Estimating emissions from crop residue open burning in China based on](#)
824 [statistics and MODIS fire products, J. Environ. Sci., 44, 158-170,](#)
825 <https://doi.org/10.1016/j.jes.2015.08.024>, 2016.

826 [Lin, Z., Chen, F., Li, B., Yu, B., Shirazi, Z., Wu, Q., and Wu, W.: FengYun-3C VIRR Active Fire](#)
827 [Monitoring: Algorithm Description and Initial Assessment Using MODIS and Landsat Data, IEEE Trans.](#)
828 [Geosci. Remote Sens., 55, 6420-6430, https://doi.org/10.1109/TGRS.2017.2728103](#), 2017.

829 [Liu, T., Marlier, M.E., DeFries, R.S., Westervelt, D.M., Xia, K.R., Fiore, A.M., Mickley, L.J., Cusworth,](#)
830 [D.H., and Milly, G.: Seasonal impact of regional outdoor biomass burning on air pollution in three Indian](#)
831 [cities: Delhi, Bengaluru, and Pune, Atmos. Environ., 172, 83–92,](#)
832 <https://doi.org/10.1016/j.atmosenv.2017.10.024>, 2018.

833 [Liu, Y., Hill, M.J., Zhang, X., Wang, Z., Richardson, A.D., Hufkens, K., Filippa, G., Baldocchi, D.D.,](#)
834 [Ma, S., and Verfaillie, J.: Using data from Landsat, MODIS, VIIRS and PhenoCams to monitor the](#)
835 [phenology of California oak/grass savanna and open grassland across spatial scales, Agric. For. Meteorol.,](#)
836 [237, 311-325, https://doi.org/10.1016/j.agrformet.2017.02.026](#), 2017.

837 [Lyapustin, A., Wang, Y., Xiong, X., Meister, G., Platnick, S., Levy, R., Franz, B., Korkin, S., Hilker, T.,](#)
838 [and Tucker, J.: Scientific impact of MODIS C5 calibration degradation and C6+ improvements, Atmos.](#)
839 [Meas. Tech., 7, 4353-4365, https://doi.org/10.5194/amt-7-4353-2014](#), 2014.

840 [Marlier, M.E., DeFries, R.S., Kim, P.S., Koplitz, S.N., Jacob, D.J., Mickley, L.J., and Myers, S.S.: Fire](#)
841 [emissions and regional air quality impacts from fires in oil palm, timber, and logging concessions in](#)
842 [Indonesia, Environ. Res. Lett., 10, 085005, https://doi.org/10.1088/1748-9326/10/8/085005](#), 2015.

843 [Matson, M. and Schneider, S.R.: Fire Detection Using the NOAA-Series Satellite, NOAA Technical](#)
844 [Report NESDIS, 7, 1984.](#)

845 [Mohajane, M., Costache, R., Karimi, F., Pham, O.B., Essahlaoui, A., Nguyen, H., Laneve, G., and Oudija,](#)
846 [E.: Application of remote sensing and machine learning algorithms for forest fire mapping in a](#)
847 [Mediterranean area, Ecol. Indic., 129, 107869, https://doi.org/10.1016/j.ecolind.2021.107869](#), 2021.

848 [Moritz, M.A., Parisien, M.A., Batllori, E., Krawchuk, M.A., Van Dorn, J., Ganz, D.J., and Hayhoe, K.:](#)
849 [Climate change and disruptions to global fire activity, Ecosphere, 3, 1–22, https://doi.org/10.1890/ES11-](#)
850 [00345.1](#), 2012.

851 [NASA FIRMS: MODIS fire products MYD14A1 V6.1 2019 \[data set\], available at:](#)
852 <https://firms.modaps.eosdis.nasa.gov/map/>, last access 10 January 2021.

853 [NSMC: FY-3D fire products 2018-2019 \[data set\], available at:](#)
854 <http://satellite.nsmc.org.cn/portalsite/default.aspx>, last access 10 January 2021.

855 [Oliveira, M., Delerue-Matos, C., Pereira, M.C., and Morais, S.: Environmental Particulate Matter Levels](#)
856 [during 2017 Large Forest Fires and Megafires in the Center Region of Portugal: A Public Health Concern?](#)
857 [Int. J. Environ. Res. Public Health, 17, 1032, <https://doi.org/10.3390/ijerph17031032>, 2020.](#)

858 [Sayer, A., Hsu, N., Bettenhausen, C., Jeong, M.J., and Meister, G.: Effect of MODIS Terra radiometric](#)
859 [calibration improvements on Collection 6 Deep Blue aerosol products: Validation and Terra/Aqua](#)
860 [consistency, J. Geophys. Res.-Atmos., 120, 12.157-112.174, <https://doi.org/10.1002/2015JD023878>,](#)
861 [2015.](#)

862 [Schroeder, W., Oliva, P., and Giglio, L.: The New VIIRS 375 m active fire detection data product:](#)
863 [Algorithm description and initial assessment, Remote Sens. Environ., 143, 85-96,](#)
864 [https://doi.org/10.1016/j.rse.2013.12.008, 2014.](#)

865 [Sharma, A., Wang, J., and Lennartson, E.M.: Intercomparison of MODIS and VIIRS Fire Products in](#)
866 [Khanty-Mansiysk Russia: Implications for Characterizing Gas Flaring from Space, Atmosphere, 8, 95,](#)
867 [https://doi.org/10.3390/atmos8060095, 2017.](#)

868 [Stephenson, C., Handmer, J., and Betts, R.: Estimating the economic, social and environmental impacts](#)
869 [of wildfires in Australia, Environ. Hazards, 12, 93-111, <https://doi.org/10.1080/17477891.2012.703490>,](#)
870 [2013.](#)

871 [Tian, F., Fensholt, R., Verbesselt, J., Grogan, K., Horion, S., and Wang, Y.: Evaluating temporal](#)
872 [consistency of long-term global NDVI datasets for trend analysis, Remote Sens. Environ., 163, 326-340,](#)
873 [https://doi.org/10.1016/j.rse.2015.03.031, 2015.](#)

874 [Twohy, C.H., Toohey, D.W., Levin, E.J., DeMott, P.J., Rainwater, B., Garofalo, L.A., Pothier, M.A.,](#)
875 [Farmer, D.K., Kreidenweis, S.M., and Pokhrel, R.P.: Biomass Burning Smoke and Its Influence on](#)
876 [Clouds Over the Western US, Geophys. Res. Lett., 48, e2021GL094224,](#)
877 [https://doi.org/10.1029/2021GL094224, 2021.](#)

878 [Volkova, L., Roxburgh, S.H., Surawski, N.C., Meyer, C.P., and Weston, C.J.: Improving reporting of](#)
879 [national greenhouse gas emissions from forest fires for emission reduction benefits: An example from](#)
880 [Australia, Environ. Sci. Policy, 94, 49-62, <https://doi.org/10.1016/j.envsci.2018.12.023>, 2019.](#)

881 [Wang, D., Guo, J., Chen, A., Bian, L., Ding, M., Liu, L., Lv, Y., Li, J., Guo, X., and Han, Y.: Temperature](#)
882 [inversion and clouds over the Arctic Ocean observed by the 5th Chinese National Arctic Research](#)
883 [Expedition, J. Geophys. Res.-Atmos., 125, e2019JD032136, <https://doi.org/10.1029/2019JD032136>,](#)
884 [2020.](#)

885 [Wang, D., Morton, D., Masek, J., Wu, A., Nagol, J., Xiong, X., Levy, R., Vermote, E., and Wolfe, R.:](#)
886 [Impact of sensor degradation on the MODIS NDVI time series, Remote Sens. Environ., 119, 55-61,](#)
887 [https://doi.org/10.1016/j.rse.2011.12.001, 2012.](#)

888 [Wickramasinghe, C., Wallace, L., Reinke, K., and Jones, S.: Intercomparison of Himawari-8 AHI-FSA](#)
889 [with MODIS and VIIRS active fire products, Int. J. Digit. Earth, 13, 457-473,](#)
890 [https://doi.org/10.1080/17538947.2018.1527402, 2018.](#)

891 [Wintle, B.A., Legge, S., and Woinarski, J.: After the Megafires: What Next for Australian Wildlife?](#)
892 [Trends Ecol. Evol., 35, 753-757, https://doi.org/10.1016/j.tree.2020.06.009, 2020.](#)

893 [Xie, Y., Zhang, Y., Xiong, X., Qu, J.J., and Che, H.: Validation of MODIS aerosol optical depth product](#)
894 [over China using CARSNET measurements, Atmos. Environ., 45, 5970-5978,](#)
895 [https://doi.org/10.1016/j.atmosenv.2011.08.002, 2011.](#)

896 [Xiong, X., Angal, A., Twedt, K.A., Chen, H., Link, D., Geng, X., Aldoretta, E., and Mu, Q.:MODIS](#)
897 [reflective solar bands on-orbit calibration and performance, IEEE Trans. Geosci. Remote Sensing, 57,](#)
898 [6355-6371, http://doi.org/10.1109/TGRS.2019.2905792, 2019.](#)

899 [Xu, W., Wooster, M.J., Kaneko, T., He, J., Zhang, T., and Fisher, D.: Major advances in geostationary](#)
900 [fire radiative power \(FRP\) retrieval over Asia and Australia stemming from use of Himarawi-8 AHI,](#)
901 [Remote Sens. Environ., 193, 138-149, https://doi.org/10.1016/j.rse.2017.02.024, 2017.](#)

902 [Yuchi, W., Yao, J., Kathleen, E.M., Roland, S., Radenko, P., Didier, D., Michael, D.M., and Sarah, B.H.:](#)
903 [Blending forest fire smoke forecasts with observed data can improve their utility for public health](#)
904 [applications, Atmos. Environ., 145, 308-317, https://doi.org/10.1016/j.atmosenv.2016.09.049, 2016.](#)

905 [Zhang, Z., Feng, Z., Zhang, H., Zhao, J., Yu, S., and Du, W.: Spatial distribution of grassland fires at the](#)
906 [regional scale based on the MODIS active fire products. Int. J. Wildland Fire, 26, 209-218,](#)
907 [https://doi.org/10.1071/WF16026, 2017.](#)

908 [Abram, N.J., Henley, B.J. and Sen Gupta, A.: Connections of climate change and variability to](#)
909 [large and extreme forest fires in southeast Australia, Commun. Earth Environ., 2, 8, https://doi.](#)
910 [org/10.1038/s43247-020-00065-8, 2021.](#)

911 [Alisjahbana, A.S. and Busch, J.M.: Forestry, Forest Fires, and Climate Change in Indonesia. Bu](#)
912 [ll. of Indones. Econ. Stud., 53, 111-136, https://doi.org/10.1080/00074918.2017.1365404, 2017.](#)

913 [Andela, N., Morton, D.C., Giglio, L., Paugam, R., Chen, Y., Hantson, S., van der Werf, G.](#)
914 [R., and Randerson, J.T.: The Global Fire Atlas of individual fire size, duration, speed and dire](#)
915 [ction, Earth Syst. Sci. Data, 11, 529-552, https://doi.org/10.5194/essd-11-529-2019, 2019.](#)

916 [Boles, S.H. and Verbyla, D.L.: Comparison of three AVHRR based fire detection algorithms fo](#)
917 [r interior Alaska, Remote Sens. Environ., 72, 1-16, https://doi.org/10.1016/S0034-4257\(99\)00079-](#)
918 [6-2000.](#)

919 [Cerda, Lloret, F., Ruiz, J.E., and Vandermeer, J.H.: Tree mortality following ENSO-associated f](#)
920 [ires and drought in lowland rain forests of Eastern Nicaragua, For. Ecol. Manage., 265, 248-25](#)
921 [7, https://doi.org/10.1016/j.foreco.2011.10.034, 2012.](#)

922 [Cochrane, M.: Fire science for rainforests, Nature, 421, 913-919, https://doi.org/10.1038/nature01](#)
923 [437, 2003.](#)

924 [Dozier, J.: A method for satellite identification of surface temperature fields of subpixel resolut](#)
925 [ion, Remote Sens. Environ., 74, 33-38, https://doi.org/10.1016/0034-4257\(81\)90021-3, 1981.](#)

926 [Fensholt, R., and Proud, S.R.: Evaluation of earth observation based global long term vegetatio](#)
927 [n trends—Comparing GIMMS and MODIS global NDVI time series, Remote Sens. Environ., 1](#)
928 [19, 131-147, https://doi.org/10.1016/j.rse.2011.12.015, 2012.](#)

929 Flannigan, M.D. and Haar, T.H.: Forest fire monitoring using NOAA satellite AVHRR, *Can. J.*
930 *For. Res.*, 16, 975–982, <https://doi.org/10.1139/x86-171>, 1986.

931 Giglio, L., Boschetti, L., Roy, D.P., Humber, M.L., and Justice, C.O.: The Collection 6 MODIS
932 S burned area mapping algorithm and product, *Remote Sens. Environ.*, 217, 72–85, <https://doi.org/10.1016/j.rse.2018.08.005>, 2018.

934 Guo, J., Zhang, X., Cao, C., Che, H., Liu, H., Gupta, P., Zhang, H., Xu, M., and Li, X.: Mo
935 nitoring haze episodes over the Yellow Sea by combining multisensor measurements, *Int. J. Re*
936 *mote Sens.*, 31, 4743–4755, <https://doi.org/10.1080/01431161.2010.485213>, 2010.

937 Guo, L., Ma, Y., Tigabu, M., Guo, X., Zheng, W., and Guo, F.: Emission of atmospheric poll
938 utants during forest fire in boreal region of China, *Environ. Pollut.*, 264, 114709, <https://doi.org/10.1016/j.envpol.2020.114709>, 2020.

940 Hall, J.V., Zhang, R., Schroeder, W., Huang, C., and Giglio, L.: Validation of GOES-16 ABI
941 and MSG SEVIRI active fire products, *Int. J. Appl. Earth Obs. Geoinf.*, 83, 101928, <https://doi.org/10.1016/j.jag.2019.101928>, 2019.

943 Huff, A.K., Kondragunta, S., Zhang, H., and Hoff, R.M.: Monitoring the impacts of wildfires
944 on forest ecosystems and public health in the exo-urban environment using high-resolution satel
945 lite aerosol products from the visible infrared imaging radio meter suite (VIIRS), *Environ. Heal*
946 *th Insights*, 9s2, EHS19590, <https://doi.org/10.4137/ehi.s19590>, 2015.

947 Jacobson, M.Z.: Effects of biomass burning on climate, accounting for heat and moisture fluxe
948 s, black and brown carbon, and cloud absorption effects, *J. Geophys. Res. Atmos.*, 119, 2014J
949 D021861, <https://doi.org/10.1002/2014JD021861>, 2014.

950 Jethva, H., Torres, O., and Field, R.D.: Connecting Crop Productivity, Residue Fires, and Air Q
951 uality over Northern India, *Sci. Rep.*, 9, 16594, <https://doi.org/10.1038/s41598-019-52799-x>, 201
952 9.

953 Johnston, F.H., Henderson, S.B., Chen, Y., Randerson, J.T., Marlier, M., DeFries, R.S., Kinney,
954 P., Bowman, D.M., and Brauer, M.: Estimated global mortality attributable to smoke from lan
955 dscape fires, *Environ. Health Perspect*, 120, <https://doi.org/10.1289/ehp.1104422>, 2012.

956 Kaufman, Y.J., Kleidman, R.G., and King, M.D.: SCAR-B fires in the tropics: properties and
957 remote sensing from EOS MODIS, *J. Geophys. Res. Atmos.*, 103(D24): 31955–31968, <https://doi.org/10.1029/98JD02460>, 1998.

959 Kaufman, Y.J., Setzer, A., and Justice, C.: Remote Sensing of Biomass Burning in the Tropics,
960 *Fire in the Tropical Biota*, 84, 371–399, https://doi.org/10.1007/978-3-642-75395-4_16, 1990.

961 Keegan, K.M., Albert, M.R., McConnell, J.R., and Baker, I.: Climate change and forest fires s
962 ynergistically drive widespread melt events of the Greenland Ice Sheet, *Proc. Natl. Acad. Sci.*
963 *U.S.A.*, 111, 7964–7967, <https://doi.org/10.1073/pnas.1405397111>, 2014.

964 Keeley, J.E., Bond, W.J., Bradstock, R.A., Pausas, J.G., and Rundel, P.W.: *Fire in Mediterranean*
965 *ecosystems: Ecology, evolution and management*, Cambridge University Press, Cambridge, U
966 nited Kingdom, 2011.

967 Kelly, L.T., Giljohann, K.M., Duane, A., Aquilué N., Archibald, S., and Batllori, E.: Fire and
968 biodiversity in the Anthropocene, *Science*, 370, eabb0355, <https://doi.org/10.1126/science.abb0355>,
969 5, 2020.

970 Li, F., Zhang, X., Kondragunta, S., and Lu, X.: An evaluation of advanced baseline imager fire
971 radiative power based wildfire emissions using carbon monoxide observed by the Tropospheric
972 Monitoring Instrument across the conterminous United States, *Environ. Res. Lett.*, 15, 09404
973 9, <https://doi.org/10.1088/1748-9326/ab9d3a>, 2020.

974 Li, J., Bo, Y., and Xie, S.: Estimating emissions from crop residue open burning in China based
975 on statistics and MODIS fire products, *J. Environ. Sci.*, 44, 158-170, [https://doi.org/10.1016/](https://doi.org/10.1016/j.jes.2015.08.024)
976 [j.jes.2015.08.024](https://doi.org/10.1016/j.jes.2015.08.024), 2016.

977 Lin, Z., Chen, F., Li, B., Yu, B., Shirazi, Z., Wu, Q., and Wu, W.: FengYun-3C VIRR Active
978 Fire Monitoring: Algorithm Description and Initial Assessment Using MODIS and Landsat D
979 ata, *IEEE Trans. Geosci. Remote Sens.*, 55, 6420-6430, [https://doi.org/10.1109/TGRS.2017.27281](https://doi.org/10.1109/TGRS.2017.2728103)
980 [03](https://doi.org/10.1109/TGRS.2017.2728103), 2017.

981 Liu, T., Marlier, M.E., DeFries, R.S., Westervelt, D.M., Xia, K.R., Fiore, A.M., Mickley, L.J.,
982 Cusworth, D.H., and Milly, G.: Seasonal impact of regional outdoor biomass burning on air po
983 llution in three Indian cities: Delhi, Bengaluru, and Pune, *Atmos. Environ.*, 172, 83-92, [https://](https://doi.org/10.1016/j.atmosenv.2017.10.024)
984 doi.org/10.1016/j.atmosenv.2017.10.024, 2018.

985 Lyapustin, A., Wang, Y., Xiong, X., Meister, G., Platnick, S., Levy, R., Franz, B., Korkin, S.,
986 Hilker, T., and Tucker, J.: Scientific impact of MODIS C5 calibration degradation and C6+ im
987 provements, *Atmos. Meas. Tech.*, 7, 4353-4365, <https://doi.org/10.5194/amt-7-4353-2014>,
988 2014.

989 Marlier, M.E., DeFries, R.S., Kim, P.S., Koplitz, S.N., Jacob, D.J., Mickley, L.J., and Myers,
990 S.S.: Fire emissions and regional air quality impacts from fires in oil palm, timber, and logging
991 concessions in Indonesia, *Environ. Res. Lett.*, 10, 085005, [https://doi.org/10.1088/1748-9326/10](https://doi.org/10.1088/1748-9326/10/8/085005)
992 [/8/085005](https://doi.org/10.1088/1748-9326/10/8/085005), 2015.

993 Matson, M. and Schneider, S.R.: Fire Detection Using the NOAA Series Satellite, NOAA Tech
994 nical Report NESDIS, 7, 1984.

995 Mohajane, M., Costache, R., Karimi, F., Pham, Q.B., Essahlaoui, A., Nguyen, H., Laneve, G.,
996 and Oudija, F.: Application of remote sensing and machine learning algorithms for forest fire
997 mapping in a Mediterranean area, *Ecol. Indic.*, 129, 107869, [https://doi.org/10.1016/j.ecolind.202](https://doi.org/10.1016/j.ecolind.2021.107869)
998 [1.107869](https://doi.org/10.1016/j.ecolind.2021.107869), 2021.

999 Moritz, M.A., Parisien, M.A., Batllori, E., Krawchuk, M.A., Van Dorn, J., Ganz, D.J., and Hay
1000 hoe, K.: Climate change and disruptions to global fire activity, *Ecosphere*, 3, 1-22, [https://doi.or](https://doi.org/10.1890/ES11-00345.1)
1001 [g/10.1890/ES11-00345.1](https://doi.org/10.1890/ES11-00345.1), 2012.

1002 NASA FIRMS: MODIS fire products MYD14A1 V6.1 2019 [data set], available at: [https://firms](https://firms.modaps.eosdis.nasa.gov/map/)
1003 [s.modaps.eosdis.nasa.gov/map/](https://firms.modaps.eosdis.nasa.gov/map/), last access 10 January 2021.

1004 NSMC: FY 3D fire products 2018-2019 [data set], available at: [http://satellite.nsme.org.cn/portals](http://satellite.nsme.org.cn/portalsite/default.aspx)
1005 [ite/default.aspx](http://satellite.nsme.org.cn/portalsite/default.aspx), last access 10 January 2021.

1006 Oliveira, M., Delerue Matos, C., Pereira, M.C., and Morais, S.: Environmental Particulate Matter
1007 Levels during 2017 Large Forest Fires and Megafires in the Center Region of Portugal: A Pu
1008 blic Health Concern? *Int. J. Environ. Res. Public Health*, *17*, 1032, [https://doi.org/10.3390/ijerph](https://doi.org/10.3390/ijerph17031032)
1009 [17031032](https://doi.org/10.3390/ijerph17031032), 2020.

1010 Schroeder, W., Oliva, P., and Giglio, L.: The New VIIRS 375 m active fire detection data pro
1011 duct: Algorithm description and initial assessment, *Remote Sens. Environ.*, *143*, 85-96, [https://d](https://doi.org/10.1016/j.rse.2013.12.008)
1012 [oi.org/10.1016/j.rse.2013.12.008](https://doi.org/10.1016/j.rse.2013.12.008), 2014.

1013 Sharma, A., Wang, J., and Lennartson, E.M.: Intercomparison of MODIS and VIIRS Fire Prod
1014 ucts in Khanty Mansiysk Russia: Implications for Characterizing Gas Flaring from Space, *Atmo*
1015 *sphere*, *8*, 95, <https://doi.org/10.3390/atmos8060095>, 2017.

1016 Stephenson, C., Handmer, J., and Betts, R.: Estimating the economic, social and environmental
1017 impacts of wildfires in Australia, *Environ. Hazards*, *12*, 93-111, [https://doi.org/10.1080/17477891.](https://doi.org/10.1080/17477891.2012.703490)
1018 [2012.703490](https://doi.org/10.1080/17477891.2012.703490), 2013.

1019 Suits, G., Malila, W., and Weller, T.: The prospects for detecting spectral shifts due to satellite
1020 sensor aging, *Remote Sens. Environ.*, *26*, 17-29, [https://doi.org/10.1016/0034-4257\(88\)90117-4.](https://doi.org/10.1016/0034-4257(88)90117-4)
1021 [1988](https://doi.org/10.1016/0034-4257(88)90117-4).

1022 Tian, F., Fensholt, R., Verbesselt, J., Grogan, K., Horion, S., and Wang, Y.: Evaluating tempora
1023 l consistency of long term global NDVI datasets for trend analysis, *Remote Sens. Environ.*, *16*
1024 *3*, 326-340, <https://doi.org/10.1016/j.rse.2015.03.031>, 2015.

1025 Twohy, C.H., Toohey, D.W., Levin, E.J., DeMott, P.J., Rainwater, B., Garofalo, L.A., Pothier,
1026 M.A., Farmer, D.K., Kreidenweis, S.M., and Polkrel, R.P.: Biomass Burning Smoke and Its Inf
1027 luence on Clouds Over the Western US, *Geophys. Res. Lett.*, *48*, e2021GL094224, [https://doi.or](https://doi.org/10.1029/2021GL094224)
1028 [g/10.1029/2021GL094224](https://doi.org/10.1029/2021GL094224), 2021.

1029 Volkova, L., Roxburgh, S.H., Surawski, N.C., Meyer, C.P., and Weston, C.J.: Improving reporti
1030 ng of national greenhouse gas emissions from forest fires for emission reduction benefits: An e
1031 xample from Australia, *Environ. Sci. Policy*, *94*, 49-62, [https://doi.org/10.1016/j.envsci.2018.12.0](https://doi.org/10.1016/j.envsci.2018.12.023)
1032 [23](https://doi.org/10.1016/j.envsci.2018.12.023), 2019.

1033 Wang, D., Guo, J., Chen, A., Bian, L., Ding, M., Liu, L., Lv, Y., Li, J., Guo, X., and Han,
1034 Y.: Temperature inversion and clouds over the Arctic Ocean observed by the 5th Chinese Natio
1035 nal Arctic Research Expedition, *J. Geophys. Res. Atmos.*, *125*, e2019JD032136, [https://doi.org/1](https://doi.org/10.1029/2019JD032136)
1036 [0.1029/2019JD032136](https://doi.org/10.1029/2019JD032136), 2020.

1037 Wang, D., Morton, D., Masek, J., Wu, A., Nagol, J., Xiong, X., Levy, R., Vermote, E., and
1038 Wolfe, R.: Impact of sensor degradation on the MODIS NDVI time series, *Remote Sens. Envir*
1039 *on.*, *119*, 55-61, <https://doi.org/10.1016/j.rse.2011.12.001>, 2012.

1040 Wickramasinghe, C., Wallace, L., Reinke, K., and Jones, S.: Intercomparison of Himawari 8 A
1041 HI-FSA with MODIS and VIIRS active fire products, *Int. J. Digit. Earth*, *13*, 457-473, [https://](https://doi.org/10.1080/17538947.2018.1527402)
1042 doi.org/10.1080/17538947.2018.1527402, 2018.

1043 Wintle, B.A., Legge, S., and Woinarski, J.: After the Megafires: What Next for Australian Wil
1044 dlife? *Trends Ecol. Evol.*, *35*, 753-757, <https://doi.org/10.1016/j.tree.2020.06.009>, 2020.

1045 ~~Xu, W., Wooster, M.J., Kaneko, T., He, J., Zhang, T., and Fisher, D.: Major advances in geos~~
1046 ~~tationary fire radiative power (FRP) retrieval over Asia and Australia stemming from use of Hi~~
1047 ~~marawi 8 AHI, Remote Sens. Environ., 193, 138-149, <https://doi.org/10.1016/j.rse.2017.02.024>, 2~~
1048 ~~017.~~

1049 ~~Yuehi, W., Yao, J., Kathleen, E.M., Roland, S., Radenko, P., Didier, D., Michael, D.M., and Sa~~
1050 ~~rah, B.H.: Blending forest fire smoke forecasts with observed data can improve their utility for~~
1051 ~~public health applications, Atmos. Environ., 145, 308-317, [https://doi.org/10.1016/j.atmosenv.201](https://doi.org/10.1016/j.atmosenv.2016.09.049)~~
1052 ~~[6.09.049](https://doi.org/10.1016/j.atmosenv.2016.09.049), 2016.~~

1053 ~~Zhang, Z., Feng, Z., Zhang, H., Zhao, J., Yu, S., and Du, W.: Spatial distribution of grassland~~
1054 ~~fires at the regional scale based on the MODIS active fire products. Int. J. Wildland Fire, 26,~~
1055 ~~209-218, <https://doi.org/10.1071/WF16026>, 2017.~~